

GEOSPHERE, v. 18, no. 3

<https://doi.org/10.1130/GES02458.1>

18 figures; 2 tables

CORRESPONDENCE: dlowe@mun.ca

CITATION: Lowe, D.G., DeSantis, E., Arnott, R.W.C., and Conilffe, J., 2022, Groundwater silcrete linked to brine migration in a continental rift: An alternative to the near-surface model of silcrete: *Geosphere*, v. 18, no. 3, p. 1055–1076, <https://doi.org/10.1130/GES02458.1>.

Science Editor: Andrea Hampel
Associate Editor: Michael L. Williams

Received 7 June 2021
Revision received 8 November 2021
Accepted 24 February 2022

Published online 7 April 2022

THE GEOLOGICAL SOCIETY
OF AMERICA®This paper is published under the terms of the
CC-BY-NC license.

© 2022 The Authors

Groundwater silcrete linked to brine migration in a continental rift: An alternative to the near-surface model of silcrete

David G. Lowe^{1,*}, E. DeSantis^{1,†}, R.W.C. Arnott¹, and J. Conilffe²¹Department of Earth and Environmental Sciences, University of Ottawa, 150 Louis-Pasteur Private, Ottawa, Ontario K1N 6N5, Canada²Geological Survey of Newfoundland and Labrador, P.O. Box 8700, St. John's, Newfoundland A1B 4J6, Canada

ABSTRACT

Silcretes have long been recognized as modern and ancient duricrusts, but more recently also as silicified layers precipitated at groundwater tables, termed groundwater silcrete. However, the silica sources, transport mechanisms, and precipitation processes of groundwater silcrete are not well understood, and models are limited to the near-surface groundwater environment, where silica saturation is low. Here, an example of a groundwater silcrete from Upper Cambrian strata of the Potsdam Group is described and interpreted to be formed in a rift where Cambrian fault reactivation coincided with silcrete formation. Field relationships strongly support a connection between fault activity and silicification, including a systematic thickening and development of massive silcrete horizons above shear zones, brecciated silcrete near where faults intersect shear zones, and nodules along the margins of shear zones. Petrographic and cathodoluminescence microscopy of silcrete reveal early pre-compaction overgrowth cements with abundant primary fluid inclusions. Fluid inclusion microthermometry indicates that these fluids were high salinity (22.7–25.8 eq. wt% NaCl+CaCl₂) brines with homogenization temperatures of ~120.2 °C–151.6 °C, which implies that silica precipitated from a hot, silica-saturated crustal brine from Grenville Province basement. A combination of weathering reactions and direct quartz dissolution explains the chemical evolution of the source fluid, which likely originated as infiltrated meteoric water that had chemically equilibrated with Grenville crust at depth. Later, this brine was mobilized upward along reactivated faults during the Late Cambrian, and ultimately to the water table, where a combination of reduced pH and temperature promoted quartz supersaturation and quartz overgrowths on detrital quartz. This case example, therefore, expands the definition of silcrete to include near-surface silicification from externally sourced crustal fluids, here termed brine silcrete, and provides a basis for interpreting silcrete as a feature of deformation and fluid migration along shear zones in fault-bounded continental basins.

INTRODUCTION

Silcretes are indurated layers of silica-cemented soil, sediment, or rock formed by near-surface silica precipitation (<100 m depth) related to weathering processes, groundwater flow, and diagenesis (Summerfield, 1983; Milnes and Thiry, 1992; Nash and Ullyott, 2007). Layers are well-indurated and consist of ~85–95 wt% SiO₂ in the form of overgrowths on detrital quartz, pore-filling cement, and/or replacement of clays and carbonate (Summerfield, 1983; Shaw and Nash, 1998; Nash et al., 2004). Two types of silcrete are recognized: pedogenic silcretes, which formed at and directly below subaerially exposed surfaces, and groundwater silcretes, which formed at or just below the top of the water table (Thiry et al., 1988; Milnes and Thiry, 1992; Nash and Ullyott, 2007). Pedogenic and groundwater silcrete commonly co-occur in sedimentary successions with similar microfabrics and mineralogy. However, pedogenic silcrete is differentiated from groundwater silcrete by the disruption of primary sedimentary fabrics and development of vertical soil profile organization, jointing, and peds (Thiry and Milnes, 1991; Milnes and Thiry, 1992; Nash and Ullyott, 2007).

The origin of pedogenic silcrete is relatively well understood from numerous documented examples in both modern and ancient environments. Under acidic, near-surface groundwater conditions, silica is liberated by the dissolution of clays, feldspars, and other silicates and then transported in pore fluids aided by eluviation-illuviation in the vadose zone. Silica precipitation is then driven by supersaturation promoted by evaporation. Silica precipitates in intergranular space or replaces detrital carbonate, clay, or evaporites (Summerfield, 1983; Khalaf, 1988; Thiry, 1999; Webb and Golding, 1998; Kendrick and Graham, 2004; Nash et al., 2004; Nash and Ullyott, 2007). In contrast, the origin of groundwater silcrete is much less well understood. Like pedogenic silcrete, silica dissolution is thought to be facilitated by near-surface weathering of silicates, followed by the substantial downward and lateral translocation of silica through the vadose zone to the water table. The exact chemical and physical processes leading to silica precipitation are poorly understood, but evaporation, water table fluctuations, and outflow along springs are considered key controls (Thiry et al., 1988; Shaw and Nash, 1998; Nash and Ullyott, 2007). Mass balance calculations by Thiry et al. (1988) suggest that silcrete precipitation could occur in meteoritic water with relatively low silica concentrations (~6 ppm; Morey et al., 1962) at realistic rates of groundwater flux over time periods of thousands of years. Nevertheless, this requires a remarkably stable near-surface groundwater transport

David Lowe <https://orcid.org/0000-0002-9187-5165>

*Present address: Earth Sciences Department, Memorial University of Newfoundland, 9 Arctic Avenue, St. John's, Newfoundland A1B 3X5, Canada

†Present address: Fisheries and Oceans Canada, 200 Kent Street, Ottawa, Ontario K1A 0E6, Canada

system wherein sustained and balanced silicate weathering and groundwater recharge rates coincide with sustained local conditions at the water table that act to saturate and precipitate dissolved silica.

Notably, most investigations do not consider exogenous crustal or deep basin silica sources like high temperature, high pH, silica-bearing fluids with potential silica concentrations of ~100–600 ppm (Morey et al., 1962; Dove and Rimstidt, 1994), which could dramatically increase silica flux leading to supersaturation at the water table. Similarly, direct proxies for fluid composition or temperature, like fluid inclusion thermometry, have not been used to constrain the origins of silicifying fluids in groundwater silcretes. Also, no model has yet demonstrated evidence for the role of faults in the transport of silica, despite the fact that brine and hydrothermal fluid migration along faults is well documented in modern basins (e.g., Warner et al., 2012; Hollinsworth et al., 2019) and ancient rifts (Lampe et al., 2002; Hollis et al., 2017).

Here, we test near-surface groundwater silcrete models with field- and laboratory-based observations of an ~8–142-cm-thick, silicified horizon in Cambrian strata of the Potsdam Group, deposited over the Neoproterozoic St. Lawrence Rift system near and within the Ottawa Graben. This silicified horizon, interpreted by Selleck (1978) as a pedogenic silcrete, shows a progressive thickening, silification, and brecciation toward numerous intrabasinal faults

underlain by Mesoproterozoic shear zones. These field relationships, described in detail below, suggest a role of faults as conduits for silicifying fluids. Notably also, fluid migration along faults leading to the diagenetic precipitation of apatite, calcite, sulphides, hematite, and monazite in Potsdam strata have been documented in nearby parts of the St. Lawrence Rift along the northern margin of the Adirondacks (Selleck, 2005; Allaz et al., 2013; Gall et al., 2017). To test this hypothesis, the paragenesis of silica cements and thermometry and petrography of their fluid inclusions are documented to constrain the potential sources and migration pathways of the silica-bearing fluids for this silcrete.

GEOLOGICAL SETTING

The Cambrian to Lower Ordovician Potsdam Group is a composite siliciclastic unit unconformably overlying ca. 1 Ga Grenville Province rocks across the Ottawa Embayment, a fault-bounded basin of flat-lying Paleozoic strata that fills the southern branches of the St. Lawrence Rift system, including the Ottawa Graben (Kumarapeli and Saull, 1966; Fig. 1). Ediacaran (590–577 Ma) dyke swarms and related alkaline intrusions constrain the timing of initial rifting of the St. Lawrence Rift system (Kamo et al., 1995; Cawood et al., 2001; Allen

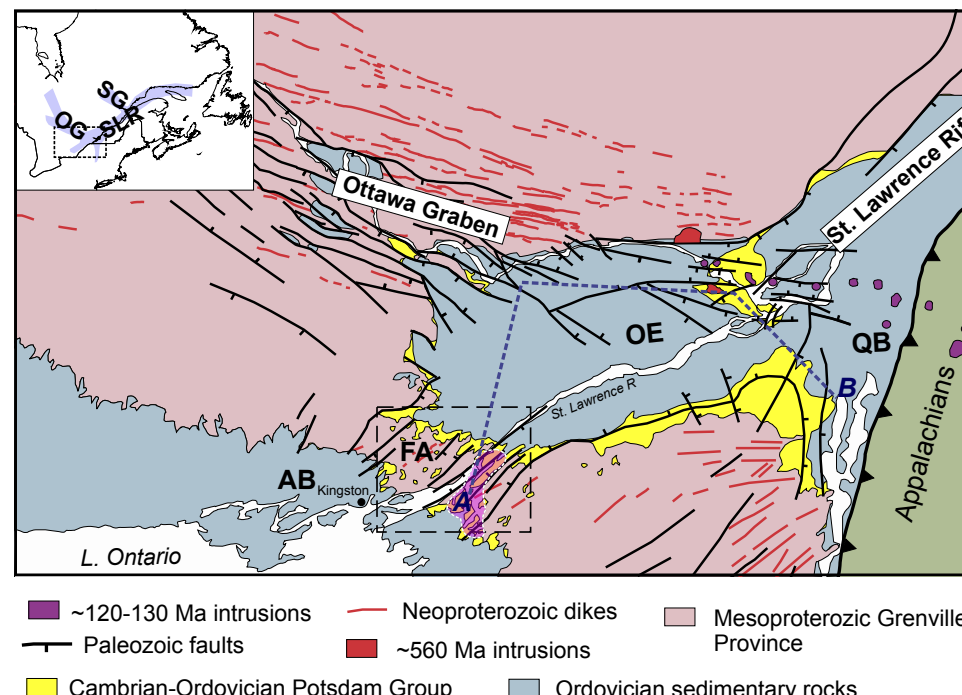


Figure 1. Map shows the Potsdam Group cropping out along the margins of the Ottawa Graben and associated parts of the St. Lawrence Rift system (shown in inset map). The current study area is shown by the black dashed box. This area, seen in more detail in Figure 3, is part of the southwest-striking extension of the St. Lawrence Rift system outlined by Paleozoic faults transected orthogonally by a later structural high termed the Frontenac Arch (FA). Paleozoic basins that cover this segment of the St. Lawrence Rift (SLR) and Ottawa graben (OG) are termed the Ottawa Embayment (OE), Quebec Basin (QB), and Appalachian Basin (AB). The silcrete distribution across the Frontenac Arch is shown under the purple polygon. The blue dashed line A–B corresponds with the stratigraphic correlation in Figure 2. SG—Saguenay graben.

et al., 2010; McCausland et al., 2011) that culminated with seafloor spreading of the proto-lapetus by 554 Ma (Kumarapeli et al., 1989). Faults in the southern St. Lawrence Rift and Ottawa Graben were subsequently reactivated repeatedly from the Paleozoic to the Cenozoic (Crough, 1981; McHone and Butler, 1984; Hogarth et al., 1988; Rimando and Benn, 2005; Salad Hersi and Dix, 2006), including during Potsdam sedimentation (Sanford and Arnott, 2010; Lowe et al., 2018).

Recent stratigraphic and provenance investigations of the Potsdam Group across the Ottawa Graben reveal a complex internal stratigraphy consisting of three unconformity-bound allounits (Allounits 1–3; Fig. 2). These record successive episodes of terrestrial and shallow marine sedimentation punctuated by erosion and unconformity development. Notably, provenance and stratigraphic data suggest these breaks in sedimentation coincided with local fault reactivation that modified basin morphology and sediment routing throughout the Ottawa Graben (Sanford and Arnott, 2010; Lowe et al., 2018). The silcrete horizon documented here caps strata of the middle allounit, termed Allounit 2, and consists of Upper Cambrian braided and ephemeral fluvial quartz arenite and quartzose conglomerate (Figs. 2–4). Based on its stratigraphic position, formation of this silcrete coincides with terminal Cambrian basin inversion and unconformity development in the Ottawa Graben (Sanford and Arnott, 2010; Lowe and Arnott, 2016; Lowe et al., 2017).

The silcrete is confined to an area south of the St. Lawrence River in northwestern New York State, USA, where it crops out along the margins of the

Frontenac Arch, a linear topographical high of Grenville basement striking northwest-southeast, and separates the Ottawa Embayment from the Appalachian Basin (Figs. 1 and 3). Here, paleogeographic reconstructions of Allounit 2 strata (Lewis, 1963; Ottos, 1966; Wolf and Dalrymple, 1984; Lowe and Arnott, 2016) and detrital zircon assemblages (Lowe et al., 2018) reveal sourcing from the east and sedimentation by northwest- to southwest-flowing braided and ephemeral streams confined between northeast-trending, fault-bounded ridges (Fig. 3). The influence of these fault-bounded ridges on Late Cambrian fluvial sedimentation is indicated by local paleoflow oriented sub-parallel to faults, boulder talus and debris flow deposits adjacent to faults (Figs. 3–4), soft sediment deformation, and thick dune and bar cross-sets that record deep flow depths in laterally confined floodplains (Lowe and Arnott, 2016).

FIELD RELATIONSHIPS

The silcrete horizon that caps quartz arenite strata of Allounit 2 crops out over an area of ~0.3 km² in northwestern New York State along the Frontenac Arch (Figs. 1 and 4–5). Here, it cross-cuts a conformable facies boundary between ephemeral and braided fluvial strata interpreted to record a change in climate from arid to humid conditions (Lowe and Arnott, 2016; Fig. 4). The horizon is 8–142 cm thick, with the thickest parts (> 130 cm) located north of

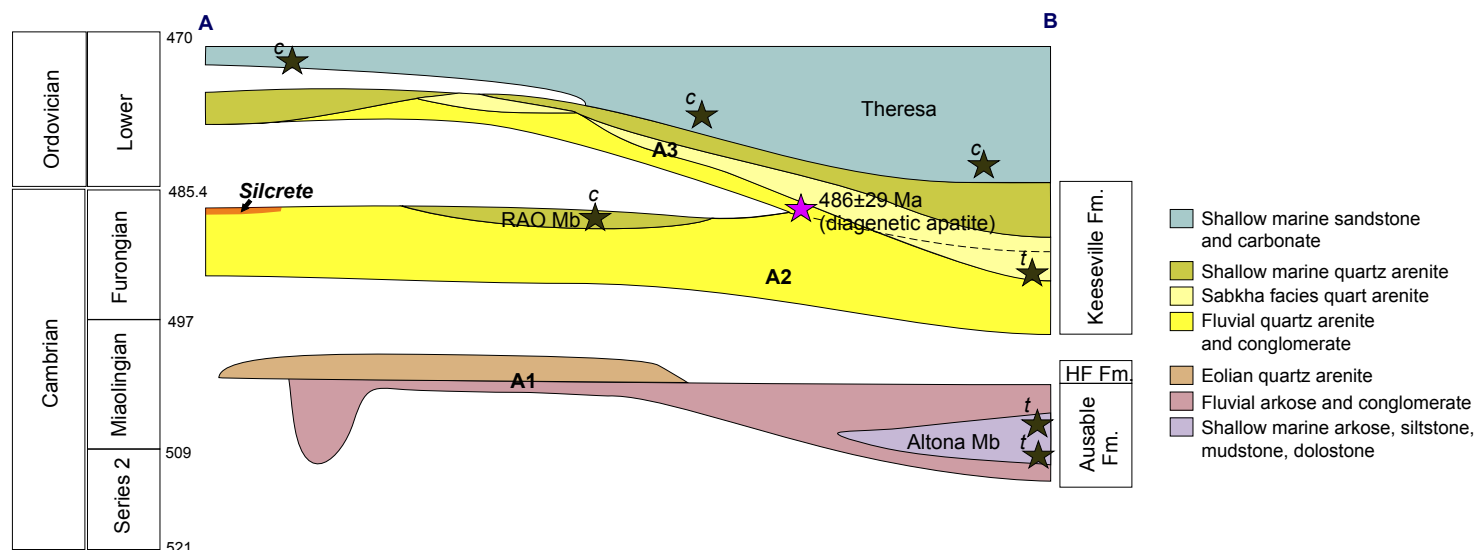


Figure 2. Stratigraphic correlation chart outlines the lithofacies and allostratigraphy of the Potsdam Group across the Ottawa Embayment and into the Quebec Basin. A–B corresponds to the dashed blue line on the geologic map in Figure 1. Age control is given by biostratigraphy (black stars) including trilobite (t) and conodont (c) faunal assemblages. For a complete list of sources, see Lowe et al. (2018). Gall et al. (2017) also provide a U-Pb age of early diagenetic apatite, shown by the purple star, with U-Pb age and error. The stratigraphic location of the silcrete is labeled and shown by the orange polygon.

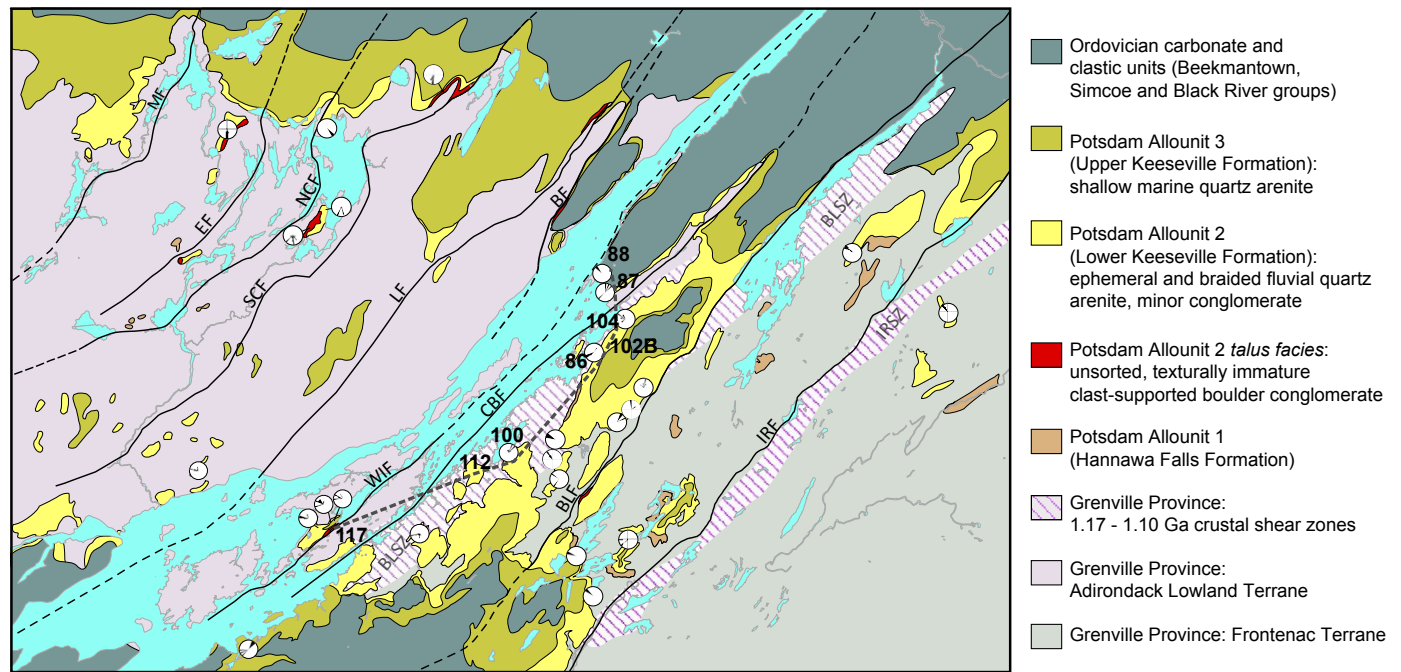


Figure 3. Geologic map shows the St. Lawrence region across the Frontenac Arch. Paleocurrent directions based on three-dimensional ripple and dune cross-stratification in Allounit 2 strata are shown by the rose diagrams. These data and the presence of local boulder talus (in red) indicate the influence of Paleozoic faults and associated fault scarps during Allounit 2 sedimentation. CBF—Chippewa Bay fault, WIF—Wellesley Island fault, BLF—Black Lake fault, IRF—Indian River fault, LF—Lyn fault, SCF—South Charleston fault, NCF—North Charleston fault, EF—Ellisville fault, MF—Muchmore fault. BLSZ—Black Lake Shear Zone, IRSZ—Indian River Shear Zone, BF—Brockville fault. The location of the stratigraphic correlation in Figure 4 is given by the dark gray dashed line, and corresponding section location numbers are given here and in Figure 5.

two prominent northeast-trending faults: Black Lake and Wellesley Island faults (Fig. 5A). Moreover, most of the exposed silcrete occurs in the fault block between the Black Lake and Chippewa Bay faults (Fig. 5A) and overlies a major shear zone in the Grenville Province termed the Black Lake Shear Zone (Figs. 3 and 5).

Silcrete texture varies across this area and includes nodular, massive, locally brecciated, and pervasively brecciated forms (Fig. 5B). Nodular forms are generally limited to the northwestern edge of the silcrete horizon north of the Wellesley Island Fault in a series of north-south-oriented road cuts over an east-west strike length of ~1900 m (Fig. 5B). Here, quartzose nodules form a 40–120-cm-thick horizon at the top of Allounit 2 strata with abrupt lateral variations in thickness. Nodules are 4–14 cm in diameter and rounded with either a spherical or bedding-parallel elliptical shape (Fig. 6). Primary stratification including planar and cross-laminae are preserved in nodules. Nodule abundance increases upwards from ~10% near the base to 80% at the top of the horizon, where nodules coalesce to form agglomerated nodule

clusters (Figs. 6A–6B). The outer surfaces of nodules are commonly highlighted by a 0.1–10 mm rind of poorly indurated iron oxide and clay-cemented sand (Figs. 6A–6B). The thickness of these rinds increases upward in the horizon as the concentration of nodules increases, resulting in a patchwork of well-cemented nodules surrounded by a moderately cemented clay- and iron oxide-rich sand in the upper ~20–30 cm of nodular horizons (Fig. 6A).

Massive silcrete is the most widespread form, cropping out extensively between the Chippewa Bay and Black Lake faults (Fig. 5B). It is characterized by an 8–105-cm-thick, silicified horizon with a sharp, undulating base with up to 15 cm vertical relief (Fig. 7). Primary depositional structures like cross-stratification and planar lamination are preserved within the silcrete. Locally, the silcrete horizon consists of two parts; a basal ~50–90 cm layer of massive silcrete is overlain sharply by a 6–13-cm-thick, more indurated layer, which is termed here the capping layer (Fig. 7).

Locally the massive silcrete horizon is brecciated, especially within ~1 km of the Black Lake and Chippewa Bay faults and exposures in the southwest

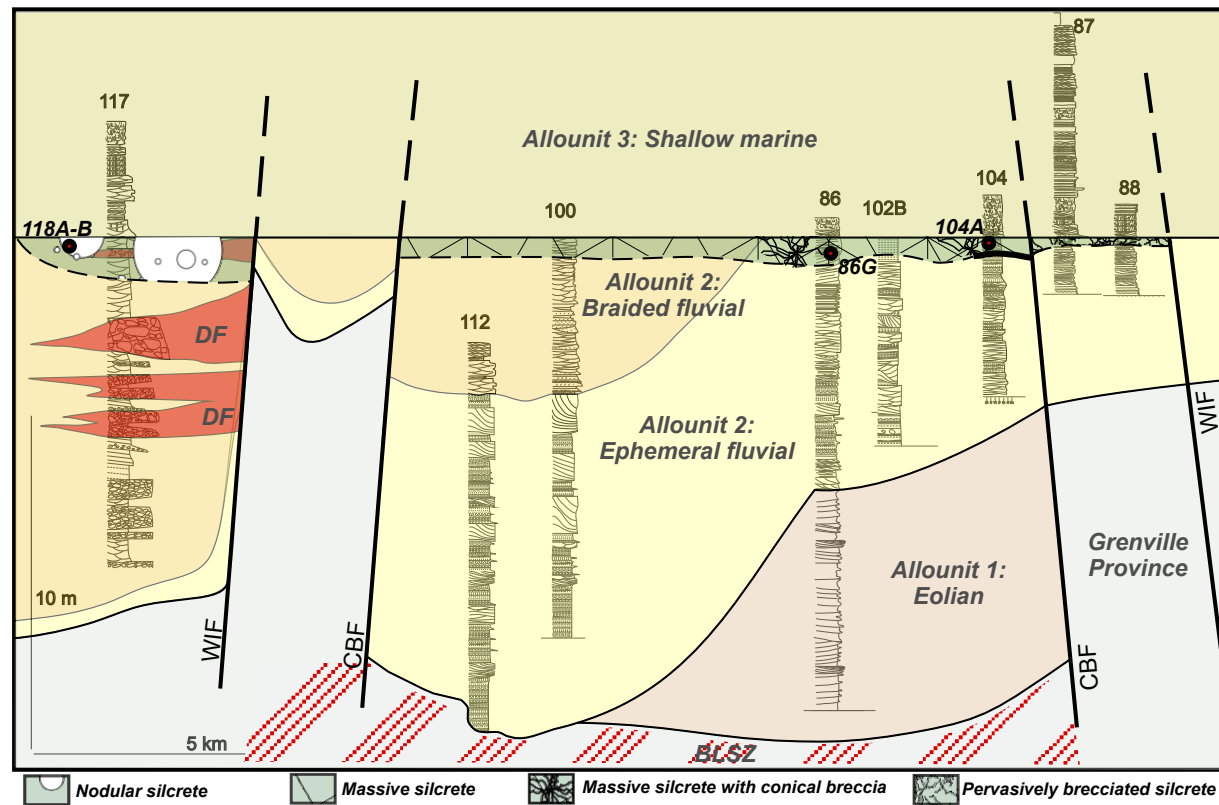


Figure 4. Stratigraphic correlation of Potsdam strata reconstructs the pre-erosional configuration of Potsdam strata with the Alluvium 2–Alluvium 3 contact as the datum. The location of the cross-section is shown in Figures 3 and 5. The stratigraphic position and distribution of the silcrete horizon along this cross-section is shown in transparent green. Note the variations in silcrete morphology and thickness, particularly across faults. CBF—Chippewa Bay fault, WIF—Wellesley Island fault, BLSZ—Black Lake Shear Zone, DF—debris flows. Numbers correspond to measured stratigraphic section locations also shown in Figures 3 and 5 and referred to elsewhere in the text and figure captions.

near the Indian River fault (Fig. 5B). Here, vertical fractures extend upward into the base of the massive silcrete, forming a complex conical network of fractures and breccia that abruptly splay out to a maximum width of ~110 cm, here termed conical breccia (Fig. 8). These features become more abundant toward the northwest in the fault block between the Chippewa Bay and Black Lake faults (Figs. 4 and 5B). At all locations, breccia cones exhibit a crude concentric zoning (Fig. 8), which from the margin inward consists of three distinct zones. Along the margins is a 3–10-cm-thick, matrix-rich breccia (mBx) consisting of 0.3–6 cm, angular to subangular, massive silcrete clasts in a 10–65% matrix of massive, distinctively dark gray weathered sandstone (Fig. 8). This zone transitions sharply to a 3–12-cm-thick layer of jigsaw-breccia (jBx)

consisting of 0.3–10 cm angular, interlocking, in situ silcrete clasts with ≤10% dark-weathered sandstone matrix filling a dense network of fractures around the clasts (Fig. 8). The silcrete clasts lack an identifiable preferred orientation, and many appear to have collapsed downward into the matrix (Fig. 8). This breccia is succeeded inward and upward by a 5–80-cm-wide core of massive but locally fractured silcrete (mS; Fig. 8). Most breccia cones do not penetrate the overlying massive silcrete but instead are deflected along its base to form a 2–6-cm-thick, matrix-rich breccia horizon that extends horizontally for 15–75 cm before either terminating gradationally into jigsaw breccia and massive silcrete or connecting to a 5–20-cm-diameter vertical breccia pipe truncated along the Alluvium 2–3 contact.

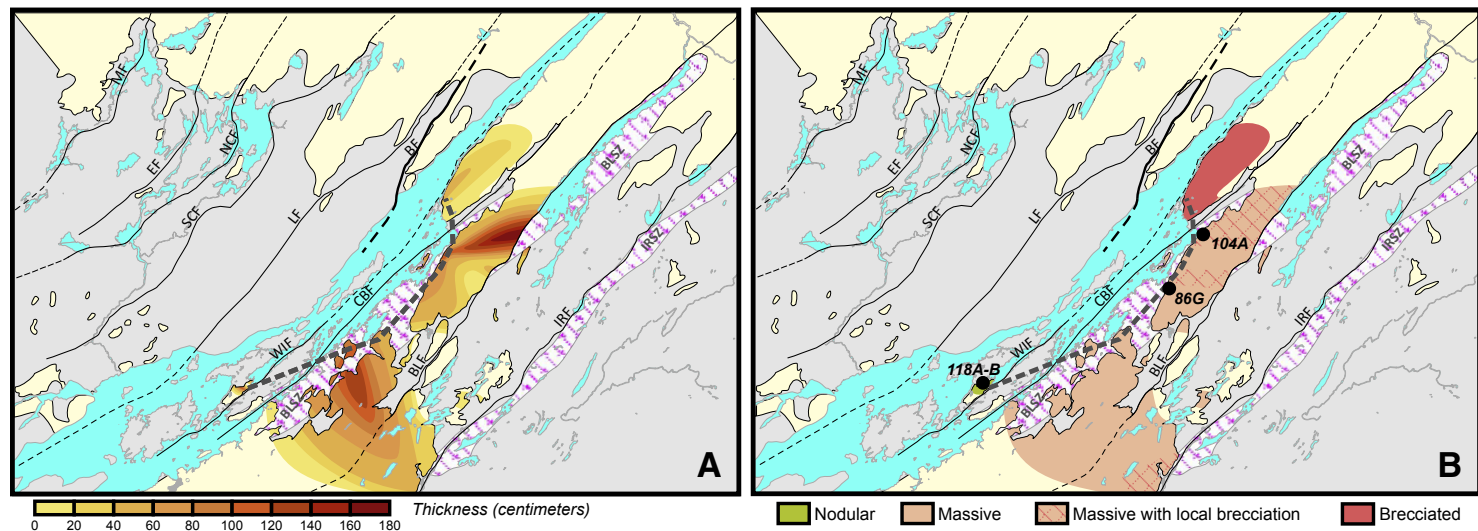


Figure 5. (A) Map shows the distribution of Allouint 2 strata (pale yellow), Paleozoic faults, underlying Grenville Province rocks, and Mesoproterozoic shear zones. Silcrete thickness contours (in centimeters) were generated manually by interpolating values of silcrete thickness values (shown on map) from outcrop sections across the Allouint 2–Allouint 3 boundary. Note that the thickest occurrences are between the Chippewa Bay fault (CBF) and Black Lake fault (BLF) and immediately north of the Wellesley Island fault (WIF); all overlie Black Lake Shear Zone (BLSZ). CBF—Chippewa Bay fault, BLF—Black Lake fault, IRF—Indian River fault, LF—Lyn fault, SCF—South Charleston fault, NCF—North Charleston fault, EF—Ellisville fault, MF—Muchmore fault, IRSZ—Indian River Shear Zone, BF—Brockville fault. (B) Map highlighting the distribution of the different textures displayed in the silcrete horizon (see text for details).

More pervasive brecciation of the silcrete is limited to the northwestern-most sections between the Chippewa Bay and Wellesley Island faults (Fig. 5B). Here, the silcrete horizon is comparatively thin—only 15–23 cm thick—with pervasive brecciation that is laterally continuous over at least 1.2 km (Figs. 3 and 5B). The pervasively brecciated horizon consists internally of alternating sheets of chaotic, matrix-rich breccia (mBx, 0.2–0.7 m wide); interlocking-jigsaw, matrix-poor breccia (jBx, 0.3–1.1 m wide); and rare 0.3–1-m-wide, massive silcrete blocks (Fig. 9). The jigsaw and matrix-rich breccia are like those in breccia cones of thicker silcrete horizons to the south, except here they consist of angular clasts that range from 0.5 cm to 16 cm wide and subangular clasts that range from 0.5 cm to 6 cm wide. These alternating breccia sheets are locally inclined ~15° to the northwest (Fig. 9).

METHODS

Silcrete Petrography

Standard optical petrography was undertaken using a polarizing microscope to determine silcrete compositions and textures. Optical photomicrographs

of silcrete samples were used to determine the apparent intergranular volume and %cement using ImageJ, an open-source image editing software. Framework grains were traced and filled in, black and color thresholds were adjusted to eliminate grains using the Global Threshold function, and residual intergranular volume was calculated using the Analyze Particles function. Percentages of other framework and matrix components were estimated visually.

Backscattered electron (BSE) imaging of thin sections was undertaken using a JEOL JSM-7100F scanning electron microscope (SEM) at Memorial University of Newfoundland, Canada, equipped with a Deben Centaurus CL detector for CL imaging and a ThermoFisher energy dispersive spectrometer (EDS) for elemental analysis. Fine-grained textures and mineralogical composition of detrital and authigenic accessory phases were determined using BSE imaging and EDS based on their electron densities and characteristic EDS spectra.

Panchromatic cathodoluminescence (CL) imaging of polished thin sections was undertaken using the JEOL JSM-7100F SEM at Memorial University of Newfoundland equipped with a Deben Centaurus CL detector, under an accelerating voltage of 15kV and a working distance of 13 mm. Based on the detection of visible and ultraviolet radiation (~300–700 nm), CL was used to reveal growth patterns in syntectonic quartz overgrowths not visible using optical or BSE imaging. In quartz, crystal lattice defects and/or impurities (e.g., substitution of Ti^{4+}

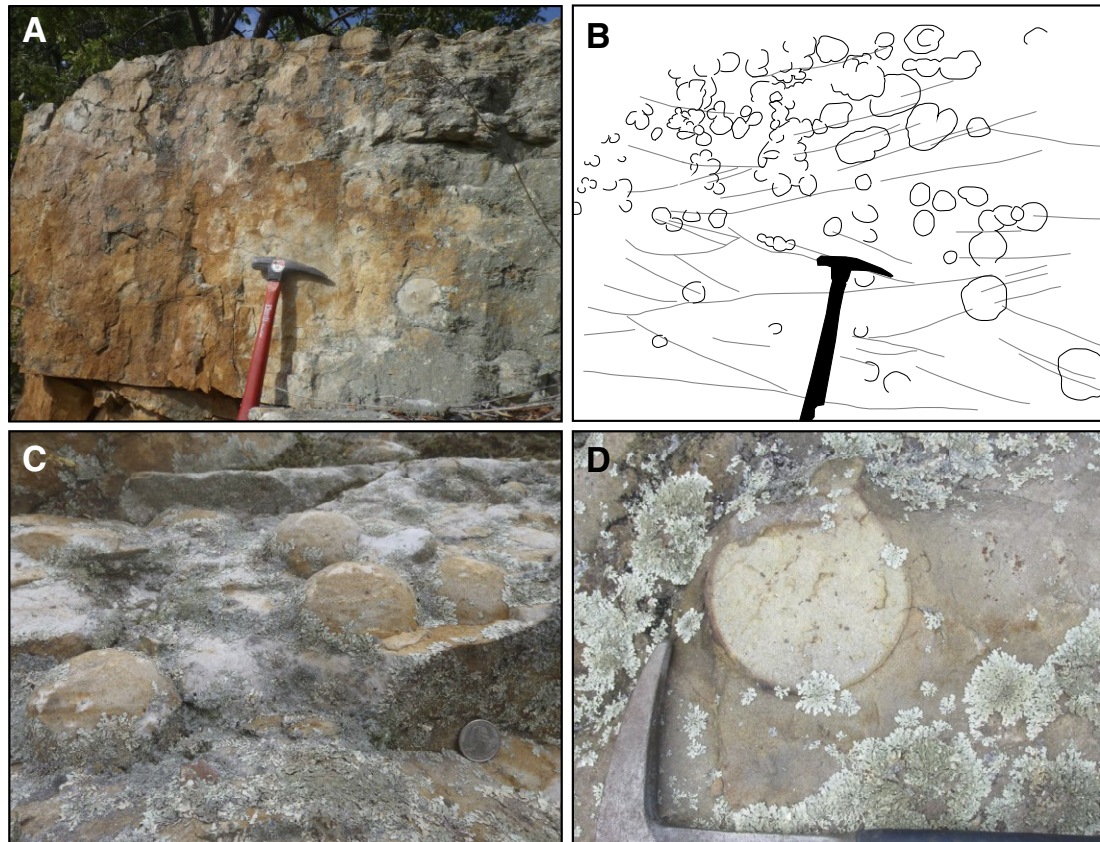


Figure 6. Photos show the nodular silcrete. (A) Nodular horizon at section 118 (Figs. 3–5), with schematic highlighting nodules and primary stratification in (B). Nodules are accentuated by thin, dark “rinds” that thicken along their tops. Nodules coalesce near the top of the horizon with nodule diameter decreasing upward. (C) Nodules exposed along a weathered and lichen-encrusted bedding plane in the middle of this horizon at section 118. (D) Bedding plane view of a nodule and rind exposed near the top of the nodular horizon at section 118.

or Ga⁴⁺ for Si⁴⁺) can result in CL as excited electrons in the crystal lattice return to their ground states (Frelinger et al., 2015).

Fluid Inclusion Analysis

Following CL imaging, five representative samples were selected to identify fluid inclusions and constrain the salinity and homogenization temperatures of fluids trapped in C1. Fluid inclusions were not found in C1.5 or C2. Double polished fluid inclusion wafers (~100 µm thick) were prepared from these samples, and petrographic description of fluid inclusions was carried out using the fluid inclusion assemblage (FIA) method and the criteria outlined in Goldstein and Reynolds (1994) and Goldstein (2003). Care was taken to focus on primary FIA trapped during cement precipitation. Numerous FIAs were also

observed in detrital quartz grains but were not included in this study since they represent inherited fluid signatures.

Microthermometric fluid-inclusion analyses at Memorial University of Newfoundland used a Linkam THMSG600 heating–freezing stage mounted on an Olympus BX51 microscope. The heating–freezing stage was calibrated using synthetic H₂O and CO₂-H₂O fluid inclusion standards, with calibration measurements at the melting point of CO₂ ($-56.6\text{ }^{\circ}\text{C} \pm 0.1\text{ }^{\circ}\text{C}$), melting point of H₂O ($0.0\text{ }^{\circ}\text{C} \pm 0.1\text{ }^{\circ}\text{C}$), and critical point of H₂O ($374.1\text{ }^{\circ}\text{C} \pm 0.5\text{ }^{\circ}\text{C}$). Following procedures outlined by Shepherd et al. (1985), the temperature of homogenization (T_h), eutectic melting temperature (T_e), hydrohalite melting temperature (T_m (hh)), and final ice-melting temperature (T_m (ice)) were measured in two-phase (liquid + vapor) inclusions. For inclusions where T_m (hh) and T_m (ice) were observed, fluid salinities (eq. wt% NaCl + CaCl₂) and molar Na/(Ca + Na) ratios were calculated using the Excel spreadsheet of Steele-MacInnis et al. (2011) for

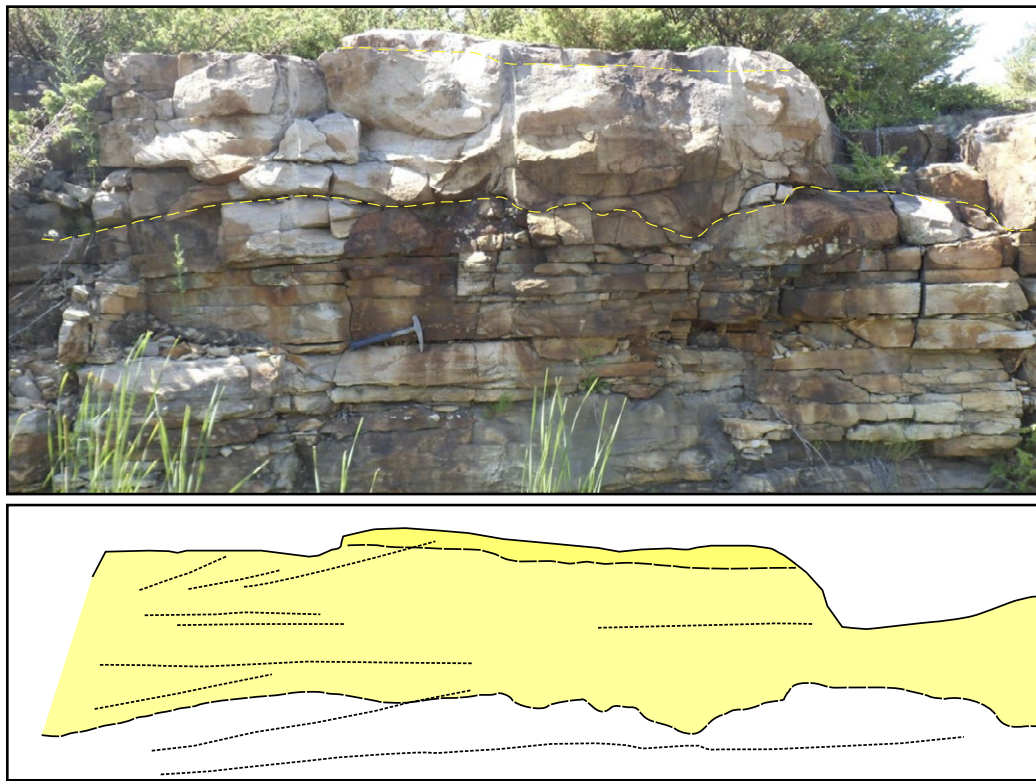


Figure 7. Photograph of the massive silcrete horizon (top) and schematic sketch (below) with the massive silcrete outlined in yellow and primary stratification outlined in light gray (section 86, see Figures 3–5). Note that primary stratification is preserved within the silcrete, and the base of the silcrete locally cross-cuts primary stratification. At this location, the massive silcrete exhibits crude layering, with a thick lower unit and a thin capping layer of more indurated silcrete (light and dark yellow, respectively).

the $\text{H}_2\text{O}-\text{NaCl}-\text{CaCl}_2$ system and reported in eq. wt% $\text{NaCl}+\text{CaCl}_2$. Salinities were also calculated using T_m (ice) and the equation of Bodnar (1993), which is used to calculate salinities as equivalent wt% NaCl (eq. wt% NaCl). Homogenization temperatures were recorded from four to six fluid inclusions in each FIA, but care was taken to ensure that all inclusions in FIA homogenized over the same temperature range to record any evidence of post-entrainment reequilibrium or modification (e.g., necking and stretching; Fall and Bodnar, 2018).

RESULTS

Optical and SEM Petrography

Nodular Silcrete

Silcrete nodules consist of well-sorted, medium- to coarse-grained, subrounded quartz grains cemented by 10–50- μm -thick syntaxial quartz

overgrowths (Fig. 10A). These overgrowths fill nearly all of the intergranular volume, which ranges from 28% to 35% of the apparent sample volume (31.5% average) with only ~2–6% porosity (Fig. 11). Point contacts dominate, and broad or sutured grain contacts are absent (Fig. 10A). Framework mineralogy is dominated by quartz that constitutes 97% to >99% of the detrital grains. Rare detrital potassium feldspar, partly altered to kaolinite, makes up to 2% percent of the framework in some samples. Accessory detrital phases include fine- to medium-grained tourmaline and fine- to very fine-grained zircon and rutile. Accessory authigenic phases associated with quartz overgrowths rimming grain boundaries include rare pyrite, illite, and ilmenite grains.

The rind that envelopes silcrete nodules (Figs. 6 and 10) varies in thickness from 0.2 mm to 3 mm near the top of the nodules to 10 μm to 200 μm near and at the base of the nodules. The thicker rind near the top of the nodules consists of sand grains dispersed in a pore-filling matrix of kaolinite, iron oxide, and quartz silt and exhibits high intergranular volume of ~25–30% (Figs. 10B and 11). In contrast, coatings near the base are 10–20- μm -thick stylolites with

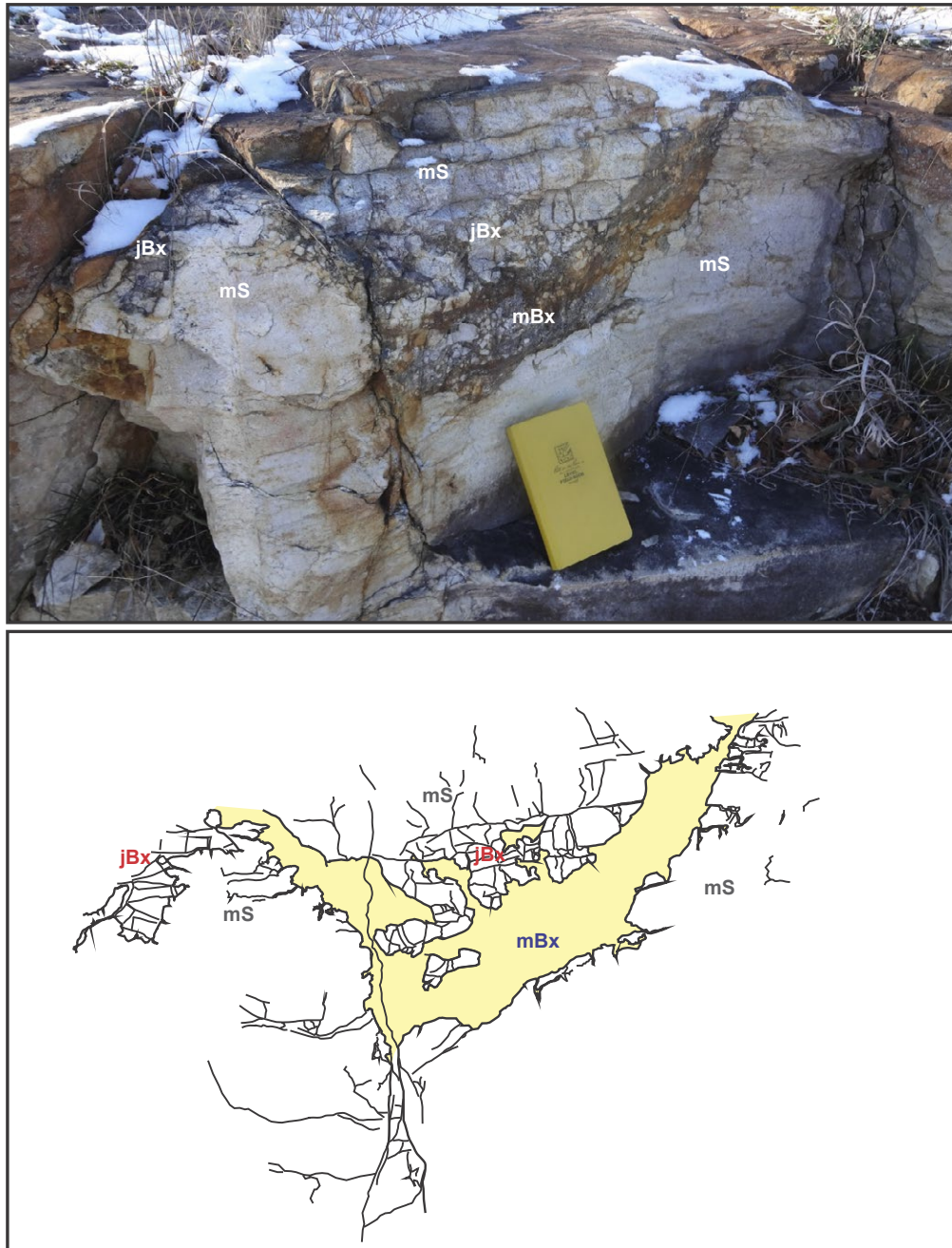


Figure 8. Typical conical breccia in a massive silcrete is exposed at section 104 (Figs. 3–5). The conical breccia widens abruptly from underlying vertical fractures in the lower part of the silcrete. Three concentric zones are recognized in the breccia: (A) MBx—massive, matrix-rich breccia forms the base of the conical breccia; (B) jBx—“jigsaw” breccia overlies the massive breccia near the center of the cone and exhibits abundant dilated fractures that envelope *in situ* clasts of silcrete; mS—massive silcrete with low fracture density forms in the center of the breccia cones and in the silcrete outside of the breccia cones.

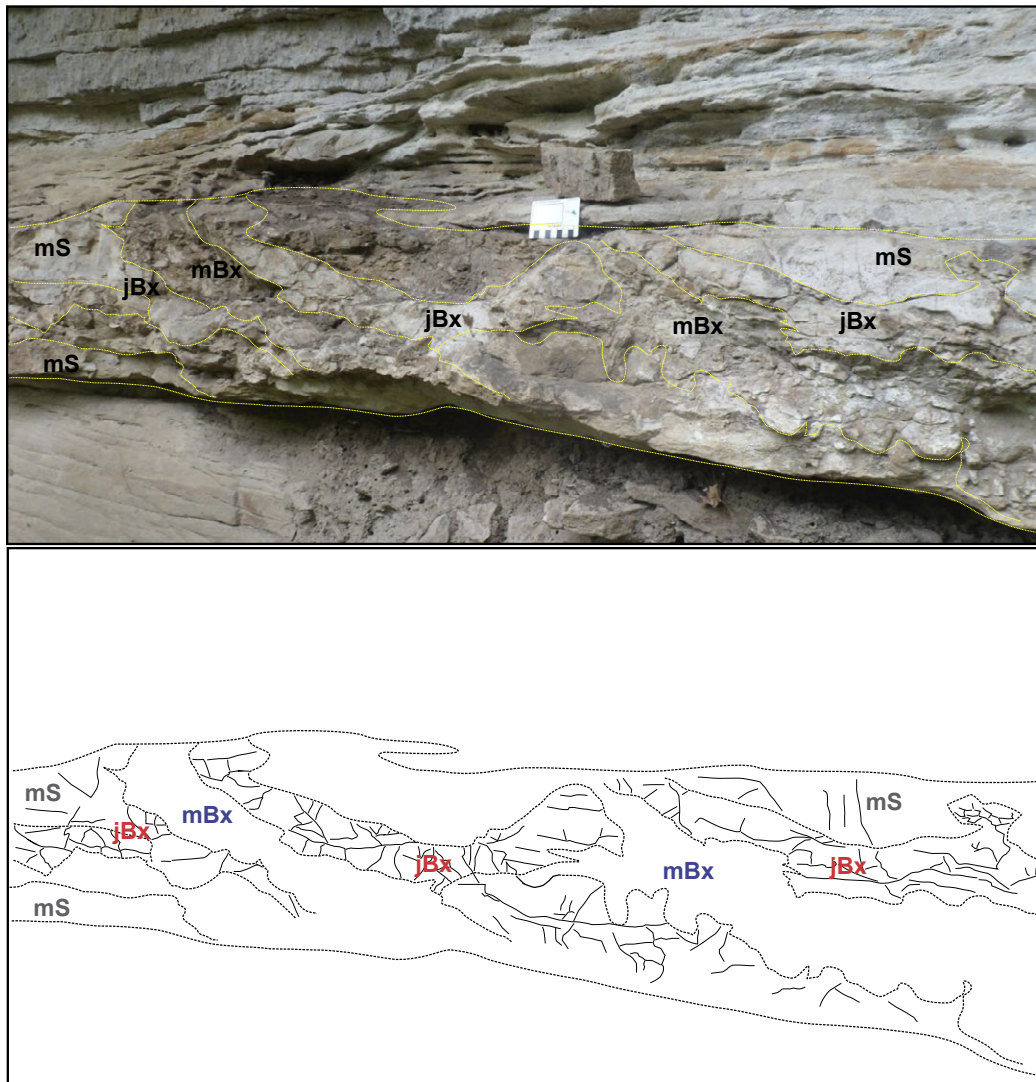


Figure 9. Pervasive brecciation forms breccia "sheets" at section 88 (see Figs. 3–5). Here, the horizon consists of sheets of chaotic massive breccia (mBx) dipping at ~15° northwest that alternate with jigsaw breccia (jBx) defined by *in situ* silcrete clasts bounded by fractures to form a high-density fracture network. Uncommon blocks of massive silcrete with minor fracturing (mS) also occur.

evidence of significant pressure dissolution of adjacent quartz grains and consist of very fine-grained TiO_2 and silt-sized apatite and zircon (Fig. 10C). The inter-nodular sandstone surrounding the nodules has the same detrital composition as the nodules, but it has lower intergranular volume and contains ~2–10% interstitial kaolinite and iron oxide, and ~5% quartz overgrowths, some of which fill large voids (Fig. 10D).

Massive Silcrete

Samples from the massive horizon are compositionally similar to the interior of nodules and consist of rounded detrital quartz grains cemented by syntactic quartz overgrowths. Apparent intergranular volume is the same as that in nodules, ranging between 28% and 35%, (Fig. 12A). Sutured contacts are absent,

but point contacts are common and some broad grain contacts are present. The framework and accessory detrital and authigenic phases in the massive horizon are the same as in the nodules described above except that feldspar is absent.

Baseline Allounit 2 Sandstone

Several samples were selected from underlying and adjacent exposures of Allounit 2 sandstone to establish a baseline for host rock composition and

texture compared with the silcrete. These samples are quartz arenite with quartz grains making up ~97% to >99% of the framework mineralogy (Fig. 12B). Feldspar is rare, and where present it makes up only ~2–3% of the framework mineralogy and is partly altered to clay minerals. These samples have an intergranular volume of 14–25%, which is filled with a mixture of ~5–20 μm quartz overgrowths, ~2–10% interstitial kaolinite and clay-sized iron oxide, rare carbonate cement, and ~1–3% porosity. Point and sutured grain contacts are common. Notably, quartz grains are also commonly fractured, unlike in the silcrete (Fig. 12B).

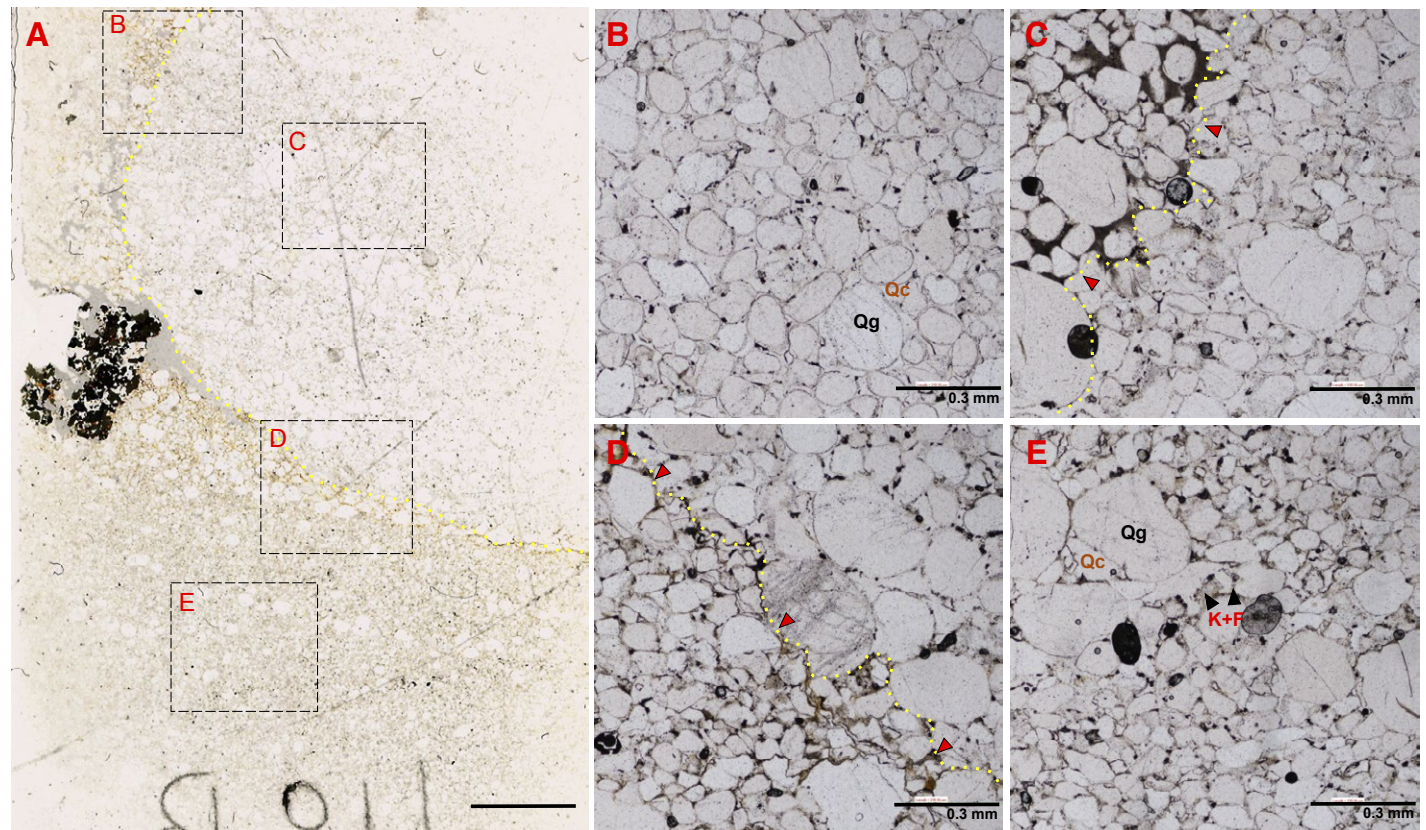


Figure 10. (A) Thin section scan (left) and photomicrographs (B–E) of nodular silcrete are shown. Boxes in panel A mark the locations of the photomicrographs. The large, dark lithic clast adjacent to the nodule consists of tourmaline and quartz. (B) Photomicrograph of the nodule interior, which consists of detrital quartz grains (Qg) cemented by syntaxial quartz overgrowths (Qc) that preserve an open-packed granular framework with high intergranular volume. (C) The upper surface of the nodules is draped by sand with abundant fine-grained, interstitial kaolinite, hematite, and fine quartz silt that preserve a high intergranular volume framework, as shown here (red arrows point to the edge of the nodule that is highlighted by the yellow dashed line). (D) Base of the same nodule shows a stylolithic contact that formed from pressure dissolution of quartz grains. (E) Photomicrograph of the surrounding quartz arenite. Some locally thick, void-filling quartz overgrowths (Qc) are present, but quartz overgrowths are typically thin here, and there is abundant interstitial matrix consisting of kaolinite, hematite, and quartz silt (K+F).

Average Intergranular volume (%) at study sites

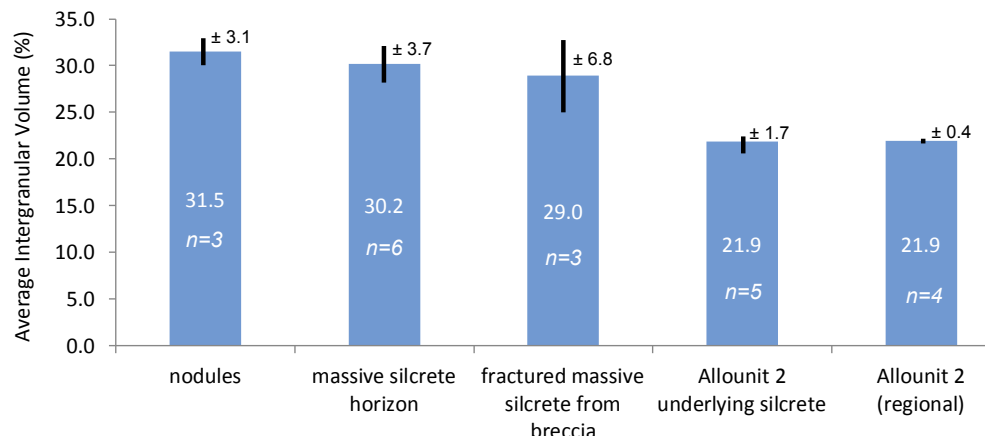


Figure 11. Bar chart shows the average intergranular volume (%) of samples of silcrete and underlying and regional baseline Allounit 2 sandstone. The intergranular volume was calculated using ImageJ by manually tracing and filling in grains in photomicrographs, thresholding to remove grains, and using the Analyze Particle function to determine the percentage of the area covered by intergranular volume.

Silcrete Breccia

Several samples were taken from conical breccia at the boundary between the jigsaw and matrix-rich breccia zones. These samples reveal clasts that are mineralogically and texturally identical to samples of the massive silcrete, which confirms their origin as intraformational clasts. The outer boundaries of the clasts tend to be broken along grain boundaries, but some sharply truncate grains and C1 overgrowths (Fig. 12C). The matrix consists of medium-grained sandstone with a moderately well-sorted framework of quartz grains surrounded by ~10–30% clay-sized iron oxide and kaolinite and admixed quartz and heavy mineral silt that is similar to the top part of the rinds that coat the nodules described above (Fig. 12D). Point and sutured contacts are common, and quartz overgrowths are rare. Compared to the grains in the adjacent massive silcrete clasts, grains in the breccia matrix are subangular, and some have jagged edges that indicate breakage and/or dissolution. Internal fractures in grains are common.

CL Petrography

CL imaging of samples from silcrete nodules and the massive silcrete revealed up to three generations of optically continuous quartz overgrowths termed C1, C1.5, and C2. These generations were identified based on luminosity domains that outlined early zoned luminous grain-rimming overgrowths (C1), an intermediate luminous void-filling cement (C1.5), and a late non-luminous, void-filling cement (C2). Both C1 and C1.5 cements luminesce but with a clear distinction in their relative timing, morphology, thickness, and zoning. C1 is a grain-coating cement consisting of ~10–40-µm-thick, euhedral or subhedral

quartz overgrowths and occurs in all samples of nodules and massive silcrete. It exhibits concentric zoning consisting of ~2–10-µm-thick alternating zones of high and low luminosity (Figs. 13A–13C). Though similarly luminous and optically continuous, C1.5 discordantly succeeds C1 in CL, filling most of the remaining interstices and occluding spaces up to 120 µm in diameter (Fig. 13C). Where present, it is significant, making up 15–25% of the sample volume. Unlike C1, C1.5 is entirely euhedral and exhibits sector zoning consisting of 10–40-µm-thick trapezoidal zones of varying luminosity (Fig. 13C). Also, C1.5 is not ubiquitous like C1; it is only recognized in one nodule sample and one sample from the massive horizon, and in the less silicified sandstone surrounding nodules in the nodular silcrete horizon. Here, C1.5 fills larger voids not already occluded by clay and iron oxide (Fig. 10D). C2 is a non-luminescing euhedral quartz overgrowth cement that postdates optically continuous C1 and C1.5, filling any remaining void space (Figs. 13A–13C). Where C1.5 is absent, C2 is a major constituent of the silcrete, filling almost all of the intergranular volume and comprising up to 25% of the sample volume.

Several samples of matrix breccia were also imaged using CL. This revealed that many of the subangular quartz grains were rimmed or partly rimmed by C1 cement. The C1 cement appears to be locally truncated by corroded margins, which suggests that a phase of silica disaggregation and dissolution occurred during or after brecciation (Fig. 13D).

Fluid Inclusion Analysis

In all samples, FIA are common in C1 quartz overgrowths within 10–45 µm of the margins of detrital quartz grains, which indicates that fluids were

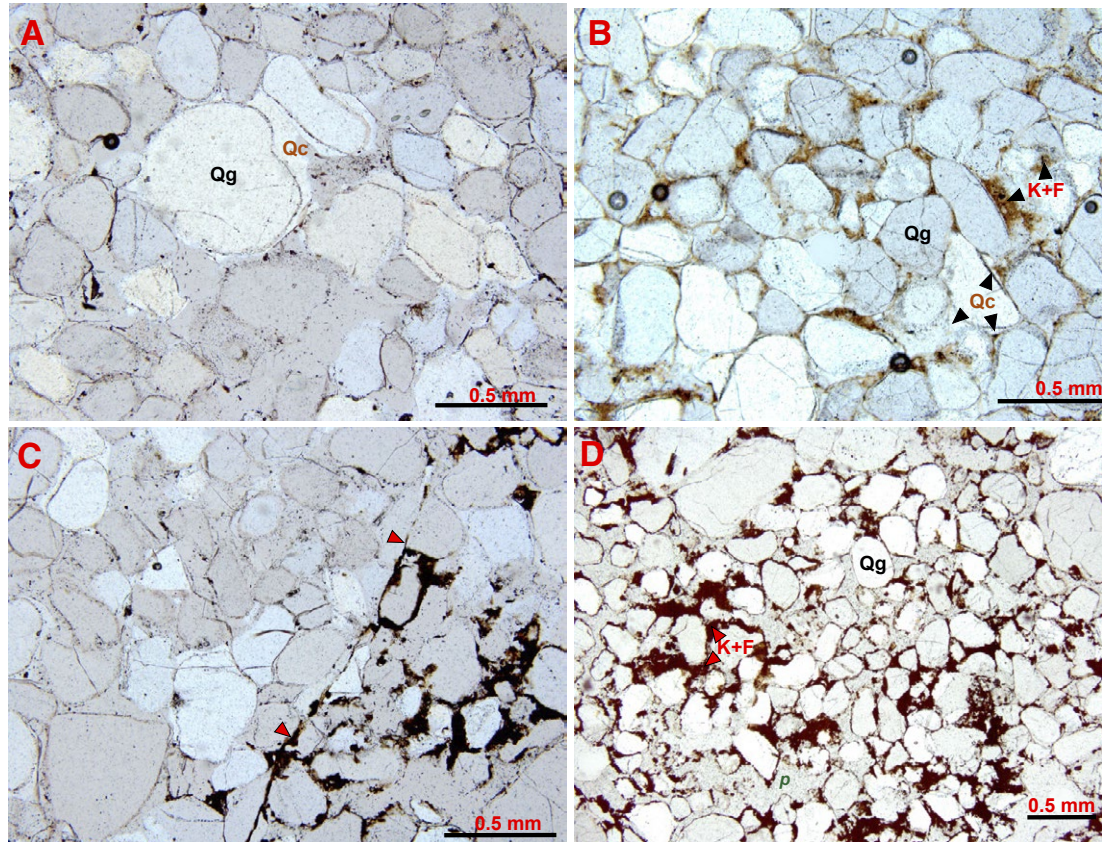


Figure 12. (A) The massive silcrete horizon is compositionally similar to the interior of nodules, with widespread syntaxial overgrowths comprising 25–31% of the sample. (B) The “baseline” Allouunit 2 sandstone has lower intergranular volume that is largely filled with interstitial kaolinite and hematite (K+H). (C) Red arrowheads point to the edge of a massive silcrete clast (left side of photomicrograph) along the margin of the jigsaw-type breccia (jBx in Figs. 8–9), where it is in contact with matrix-rich breccia (MBx in Figs. 8–9). Note the truncation of quartz grains and associated silcrete overgrowths in the silcrete clast. (C–D) The matrix of the matrix-rich breccia is shown and consists mainly of subangular quartz grains with similar sorting as in the massive silcrete but with a disorganized fabric and relatively high intergranular volume that is filled largely by kaolinite and hematite (K+H), and porosity. Qg—detrital quartz grains; Qc—void-filling quartz overgrowths.

trapped during the precipitation of C1 cement. Away from the grain boundaries, C1.5 and C2 are typically clear with no observable FIA. Fluid inclusions in C1 cement have remarkably similar petrographic and microthermometric characteristics in all samples. At room temperature, fluid inclusions in C1 cements are two-phase (liquid + vapor) and rich in liquid (~5–15% vapor). They are generally small (< 5 µm), but rare inclusions of up to 20 µm wide are also observed (Fig. 14).

Microthermometric analyses were obtained from 58 primary fluid inclusions from 15 FIAs (Figs. 15–16, Table A2). Upon cooling to –100 °C, inclusions freeze at ~–70 °C to –80 °C, forming a brown granular ice, which is consistent with high-salinity fluids (> 20 eq. wt% NaCl; Wilkinson, 2017). Some low-temperature metastable phase transition was observed, but first melting (T_m) was observed close to the eutectic temperature of the $\text{H}_2\text{O-NaCl-CaCl}_2$ system (~–52 °C; Fig. 16). T_m (hh) occurred prior to ice melting between –40.1 °C and

–36.8 °C and final ice melting (T_m (ice)) between –31.2 °C and –23.2 °C. Where T_m (hh) and T_m (ice) were observed in the same inclusions, salinities of 22.7–25.8 eq. wt% NaCl+CaCl₂ were calculated with the Na/(Na+Ca) ratio and ranged from 0.11 to 0.15. For inclusions where only T_m (ice) was observed, calculated salinities range from 24.5 eq. wt% to 29.4 eq. wt% NaCl. Note, however, that salinity estimates derived using T_m (ice) and the equations of Bodnar (1993) likely overestimate true salinities by ~2–3 wt%. Upon further heating, total homogenization to the liquid phase occurred between 120.2 °C and 151.6 °C. Homogenization temperatures of all inclusions in individual FIAs was generally < 5 °C (Fig. 15), which is consistent with little or no post-entrapment reequilibration of the inclusions (Fall and Bodnar, 2018). However, some FIAs with higher T_h values show a wider range of temperatures (up to 10 °C), which indicates that necking or stretching of inclusions may have occurred in these FIAs.

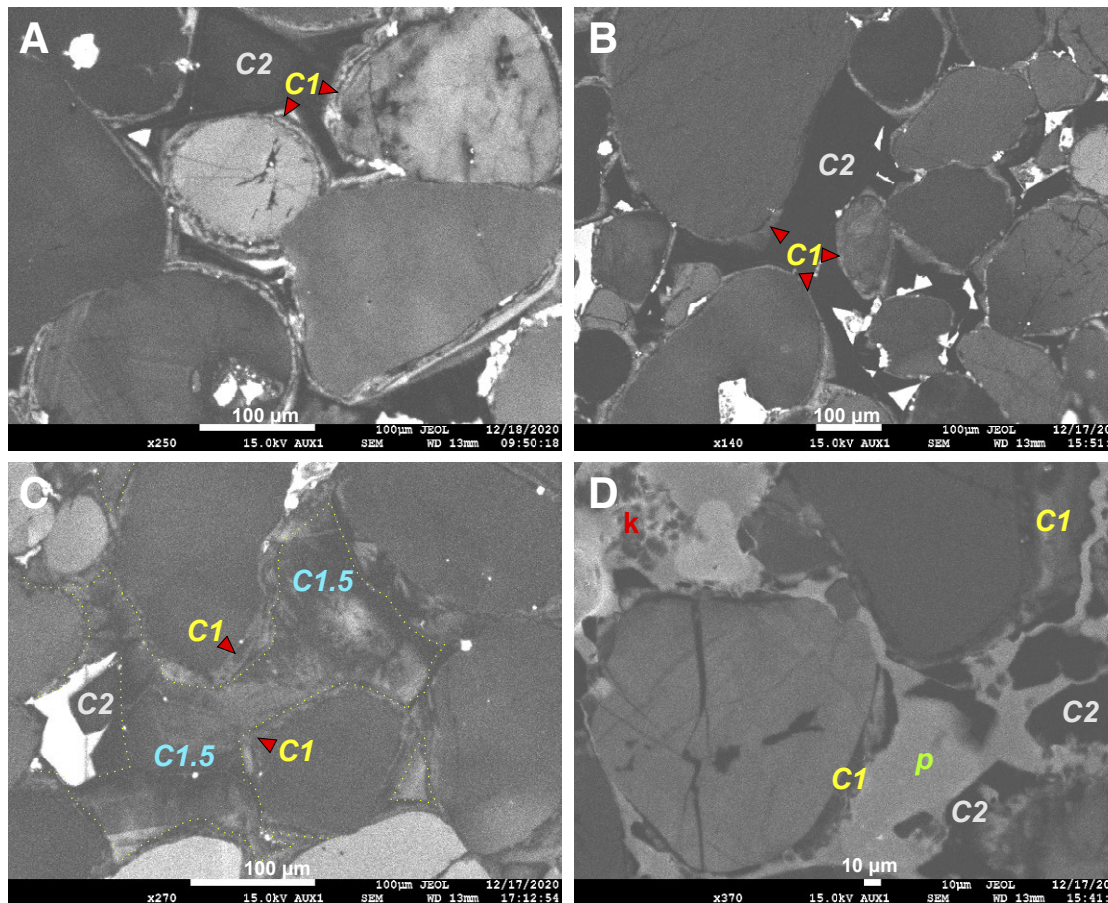


Figure 13. False-color panchromatic cathodoluminescence (CL) images of the silcrete are shown. (A) Image from the interior of a silcrete nodule shows early generation grain-coating cement, termed C1, characterized by oscillating zones of alternating luminosity. A later generation of optically continuous, non-luminescing quartz overgrowths, termed C2, fills most of the remaining void space. (B) Sample from the massive horizon shows early C1 and later C2 quartz overgrowth cement. (C) Some silcrete samples, like this example from a massive horizon, exhibit three generations of overgrowth, including C1, C2, and an intermediate zoned and luminous C1.5. (D) CL image from the breccia matrix shows corroded C1 overgrowths and void-filling C2. k—kaolinite, p—porosity.

■ DISCUSSION

Silcrete Paragenesis

Optical and CL petrography reveal a clear sequence of overgrowth genesis, with early grain-coating C1 overgrowths succeeded locally by C1.5 and everywhere by late-stage, pore-filling C2 (Figs. 13 and 17). Notably, the higher intergranular volume of C1- and C1.5-cemented silcrete (29–35%) compared to that of the underlying and regional baseline Allounit 2 strata (~22%) suggests that C1 and C1.5 pre-date more widespread porosity loss in the Allounit 2 strata. Moreover, silcrete lacks the abundant fractured grains and sutured grain contacts present in Allounit 2 samples that indicate widespread mechanical compaction and pressure solution. C1 and C1.5 overgrowths, therefore, represent a relatively

early near-surface cement that precipitated after only minor mechanical compaction coinciding with a loss of < 6% porosity from a probable initial porosity of ca. 35% (e.g., Pryor, 1973; Selley, 1978). Early C1 overgrowths likely provided local structural rigidity to the sandstone framework that counteracted the effects of compaction during burial, including pressure solution. This early timing is also demonstrated by the basal contacts of C1-cemented nodules, which are marked by localized stylolites that are lined with residual insoluble TiO₂, suggesting that nodules formed prior to compaction and pressure solution (Figs. 10 and 17).

Non-luminescing C2 overgrowths are present in all samples. C2 overgrowths fill much of the remaining intergranular volume in nodules and the massive horizon and are present as a grain-rimming overgrowth cement throughout baseline Allounit 2 samples. C2 was likely coeval with or post-dated pressure solution since it is the only overgrowth cement in compacted baseline Allounit 2 sandstone,

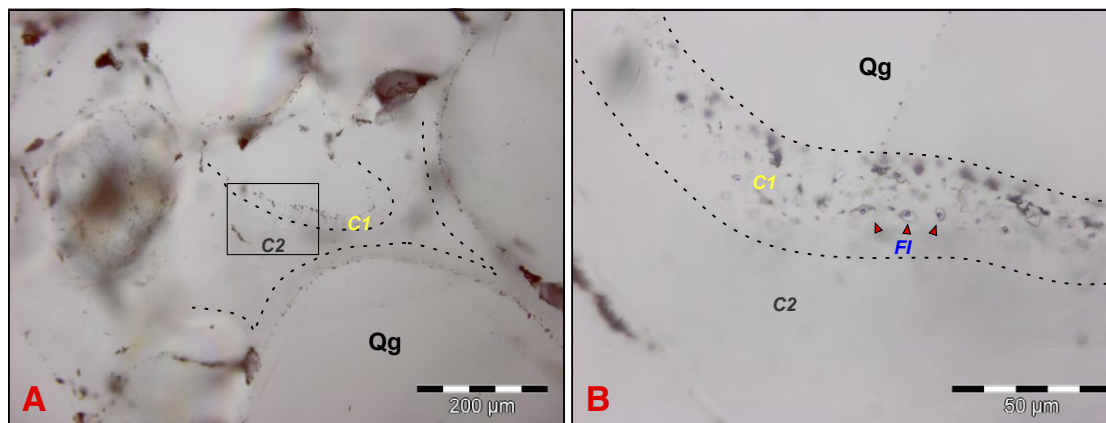


Figure 14. Plane-polarized light photomicrograph of fluid inclusions in C1 cement shows abundant two-phase inclusions in grain rimming C1. (A) Fluid inclusions are particularly abundant within 20–40 μm of grain boundaries within C1 cements. Inset rectangle outlines the location of (B), which is a close-up of two-phase fluid inclusions (FI) in C1 that range from ~1–8 μm in diameter. Qg—detrital quartz grains.

where evidence of pressure solution is widespread. Moreover, its non-luminescing character suggests that it is either purer or better structured than C1 and C1.5 (Frelinger et al., 2015), which suggests that it precipitated slowly from the direct dissolution of detrital quartz in a relatively stable subsurface diagenetic environment.

Minor (2–10%) interstitial clay- to silt-sized fines, mainly kaolinite with iron oxide and fine quartz silt, occur in the intergranular volume of baseline Allouunit 2 strata and the C1.5-cemented, inter-nodular silcrete in the nodular horizon but are absent from C1-cemented silcrete. Locally, these fines form geopetal accumulations draping the tops of nodules, where they preserve an open pre-compaction, intergranular volume locally between grains (Fig. 10). This, and their absence in C1-cemented silcrete, suggests that their emplacement post-dates C1 but pre-dates compaction. Based on their geopetal form, absence in early C1-cemented silcrete, and lack of association with weathered detrital phases, these fines are interpreted to have infiltrated unconsolidated Allouunit 2 strata by eluviation through the vadose zone. These fines were most likely derived from weathering and the erosion of granite in adjacent exposed Grenville basement, given the paucity of feldspar or other silicates in Allouunit 2 that could have sourced these fines as residuum of detrital mineral weathering.

Field and petrographic relationships demonstrate that fracturing and associated brecciation post-dates initial silcrete formation and predates Allouunit 3 sedimentation. It also truncates, and thus post-dates, C1 cementation (Fig. 12C) but has an unknown timing relative to C1.5. Later, interstitial clay and iron oxide in fractures and breccia matrix most likely accumulated during the same period of eluviation–illuviation that affected baseline Allouunit 2 strata.

Silcrete Formation

Selleck (1978) interpreted this silcrete horizon as pedogenic, based on its position beneath an unconformity, evidence of subaerial exposure, and localized brecciation. However, Thiry et al. (1988) later demonstrated a second type

of silcrete, termed groundwater silcrete, that forms at the water table and is characterized by the preservation of primary stratification and an absence of vertical soil structures. Like groundwater silcrete, the Potsdam silcrete lacks the vertical profile organization, vertical jointing, peds, or glaebules typical of pedogenic silcrete (Nash and Ulliyott, 2007) and preserves primary stratification, with brecciation and illuviation postdating silcrete formation. Accordingly, the Potsdam silcrete is interpreted to be a groundwater silcrete that formed along the water table during or after Allouunit 2 sedimentation. Following its formation, the silcrete persisted and shielded Allouunit 2 succession strata from erosion associated with the Allouunit 2–3 unconformity. This is demonstrated in Figure 5, which shows that the areal distribution of the silcrete coincides with the distribution of Allouunit 2 strata across the Frontenac Arch.

In existing groundwater silcrete models from the Paris Basin and elsewhere, silica is thought to be sourced from the weathering of detrital feldspar and/or other detrital silicates in the sediment pile or adjacent basement highs (Nash and Ulliyott, 2007; see Equation [1] below). However, fluid inclusion results from C1 overgrowths that constrain silica precipitation show that these fluids have minimum trapping temperatures of ~120–150 °C and are therefore well in excess of near-surface meteoric water temperatures. Moreover, these fluids were saline, containing ~25–30% NaCl + CaCl₂, and were enriched with Ca relative to Na (Na/(Na+Ca) of 0.11–0.15). The occurrence of minor pyrite, illite, and K-feldspar associated with C1 overgrowths further suggests that these fluids contained some HS⁻ and K⁺. Fluid inclusions in C1 cement have remarkably similar petrographic and microthermometric characteristics in all samples and likely represent a single fluid event. Of the potential crustal fluid reservoirs, the homogenization temperatures and Na/(Na/Ca) ratios are uncharacteristic of higher-temperature metamorphic or magmatic-geothermal fluid sources (Yardley and Bodnar, 2014). However, both fluid temperature and chemistry are similar to those of documented crustal brines formed by the equilibration of externally sourced fluids with crystalline basement adjacent to or underlying continental basin sediments (Carpenter et al., 1974; Bodnar et al.,

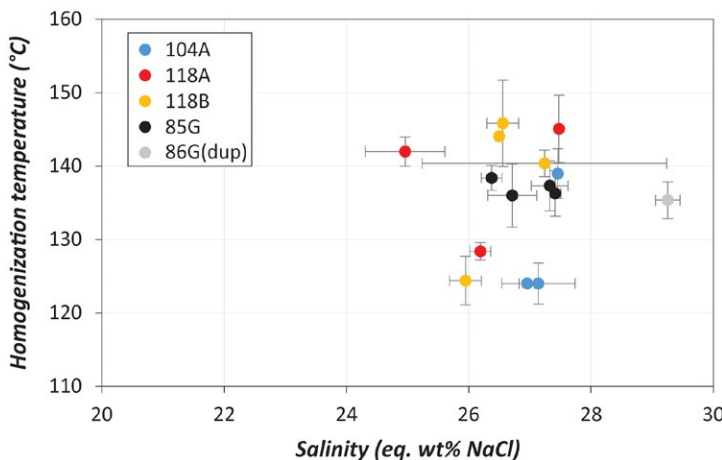


Figure 15. Cross-plot shows the homogenization temperatures and corresponding salinity estimates of C1 in an individual fluid inclusion assemblage (FIA) derived from T_m (ice) using the equations of Bodnar (1993). Filled symbols represent average values; error bars represent standard deviation within FIA. Homogenization temperatures of ~130–150 °C and corresponding salinity estimates of ~24–32 wt% NaCl suggest a relatively hot brine source.

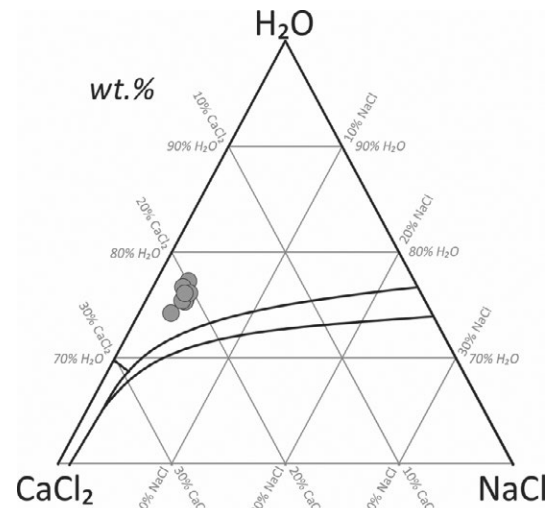
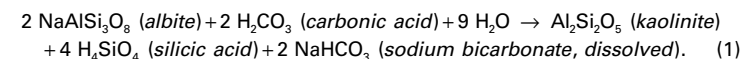


Figure 16. Ternary H₂O-NaCl-CaCl₂ plot (wt%) shows fluid compositions calculated using T_m (hh) and T_m (ice) and the spreadsheet provided by Steele MacLennan et al. (2011). Data presented from nine fluid inclusion assemblages (FIAs) in five samples show the remarkable consistency in fluid composition in all samples.

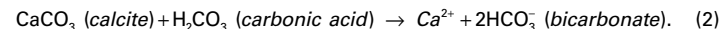
2014; Yardley and Bodnar, 2014). In this case, the most likely origin of crustal brines is meteoric water that infiltrated faults and fractures following Neoproterozoic and/or Early Cambrian rifting. These brittle faults were continuous with deeper structural fluid conduits in the pre-existing Mesoproterozoic Black Lake and Indian River Shear Zones (Figs. 4–5; Wong et al., 2011) and facilitated meteoric water infiltration to deeper levels, where it underwent extensive wall rock equilibration and heating. Considering geothermal gradients of 20 °C/km to 40 °C/km for rifted continental crust (Bertotti et al., 1999; Njiru et al., 2019), the T_h of C1 fluid inclusions suggests that fluids could have infiltrated to a depth of ~3 km, similar to fluids documented in the modern Basin and Range Province of the southwestern U.S. (Haines et al., 2016).

The evolution from mildly acidic meteoric water to high-salinity, silica-bearing brines can be explained by the chemical evolution of meteoric water that infiltrated the local Grenville upper crust, which in this area consists mainly of marble, metapelite, quartzite, granite, and rare anhydrite meta-evaporites (Whelan et al., 1990; Wong et al., 2011). For example, albite and calcite dissolution by infiltrated meteoric fluids is envisaged to have occurred during interaction with granite and marble, respectively, resulting in increased salinity (addition of Na⁺ and Ca²⁺) and pH (addition of bicarbonate).

Albite dissolution (modified from Blum and Stillings, 1995) is as follows:



Calcite dissolution is as follows:



Sources of requisite Cl⁻ for Na⁺ and Ca²⁺ complexes are more difficult to identify but could have been sourced from Grenville basement meta-evaporites (Whelan et al., 1990) and/or Cl⁻-rich amphibole (e.g., Gilliland et al., 2021).

According to the experimental work of Morey et al. (1962), Dove and Elston (1992), and Dove and Rimstidt (1994), silica solubility increases with temperature, salinity (especially Na⁺), and pH, particularly above a pH of 9. Accordingly, as these fluids equilibrated with their granite and marble host rocks, their corresponding increase in salinity, pH, and temperature also increased the solubility of silica, leading to the direct dissolution of quartz from associated granite, quartzose metapelites, and quartzite:



Once at depth, fluids remained trapped in fractured reservoirs until renewed Late Cambrian fault reactivation (e.g., Lowe et al., 2018) resulted in local fluid overpressure, reactivation of existing shear zones, and the reopening of permeability corridors that permitted these silica-bearing fluids to migrate. Similar to the documented hydrodynamics of shallow (< 6 km) normal fault zones in the East African Rift, these fluids likely migrated due to transient episodic pulses caused by overpressure-induced seismicity in response to increased stress (e.g., Hollingsworth et al., 2019). This proposed link to fluid migration along faults is further supported by field observations, including the spatial relationship

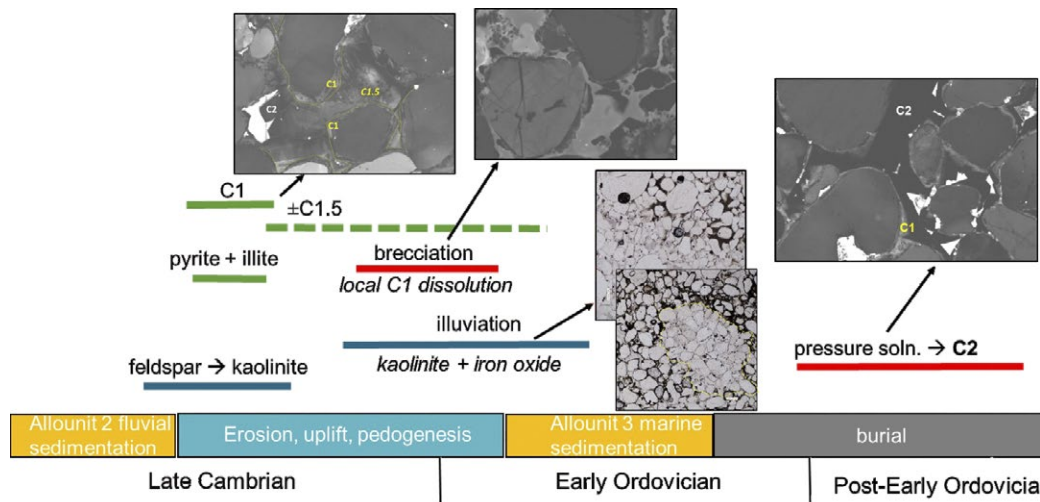


Figure 17. Schematic outlines the interpreted paragenetic sequence of silcrete cements C1, C1.5, and C2 relative to the timing of sedimentation, weathering, eluviation–illuviation, brecciation, and burial. Soln.—solution.

between faults, underlying shear zones, and silcrete texture, brecciation, and thickness (Figs. 4–5). Additionally, previous authors in other parts of the Ottawa Graben have proposed the influence of Late Cambrian and younger Paleozoic hydrothermal and/or crustal brines migrating along faults to explain occurrences of phosphate, calcite, sulphides, hematite, and monazite in Potsdam strata (Selleck, 2005; Allaz et al., 2013; Gall et al., 2017).

Following upward migration, a heated, silica-bearing crustal brine entered the water table from adjacent faults, similar to examples in the modern Suez and East African Rifts (Hollis et al., 2017; Hollinsworth et al., 2019; Fig. 18). This likely coincided with a decrease in silica solubility due to a decrease in temperature and pH during re-equilibration with near-surface temperature and atmospheric CO₂ (e.g., Selleck, 1978). Luminescence zoning at the micron-scale occurs in C1 overgrowths in nodules and massive silcrete and suggests temporal variations in compositional and/or kinetic conditions that controlled silica precipitation (Frelinger et al., 2015), which were possibly related to brine pulses and/or cycles of groundwater recharge and evaporation. Moreover, the presence of both nodular and massive silcrete forms suggests local variations in silica precipitation kinematics. The nodules lack evidence of concentric zonation or nucleation and therefore formed by pervasive rather than incremental concentric growth (Raiswell and Fisher, 2000), which suggests that nucleation site availability was not a factor in the formation of nodules. Instead, the formation of nodules is likely related to the immiscibility of the silicifying brine in groundwater. This brine-groundwater immiscibility resulted in localized sub-spherical pockets of interstitial, silica-bearing brine that precipitated quartz overgrowths as discrete nodules. In contrast, the massive horizon records either a degree of homogenization/miscibility with groundwater or the coalescence of an immiscible brine layer capping the groundwater aquifer. Either way, the key to the difference is in the flux of brine; it was higher in areas that formed massive horizons relative to

areas with nodular forms. This is consistent with the observed areal distribution of the massive and nodular horizons relative to faults; massive horizons are widespread and overlie the Black Lake Shear Zone and associated shallow faults that acted as fluid conduits, whereas nodular horizons formed in a relatively small area at the northern edge of the underlying Black Lake Shear Zone and therefore are distal to the proposed fluid conduits (Figs. 4, 5, and 17).

Silcrete Brecciation and C1 Dissolution

Silcrete breccia is in situ, and optical and CL petrography suggest that both fracture fill and matrix are composed of disaggregated silcrete with evidence of C1 dissolution (Fig. 13D). The fractures and breccia form a continuum of genetically related deformation textures that formed through varying degrees of fracturing, fluid migration, and silcrete dissolution. The three textural zones of the conical and sheet-like fracture-breccia networks (mBx, jBx, and mS; Figs. 8–9) are similar to documented textures of shear zones with high fluid flux (e.g., Hollinsworth et al., 2019), including cataclastite (= massive breccia, mBx), heavily fractured protocataclastite (= jigsaw breccia, jBx), and protocataclastite (= fractured silcrete, mS). Moreover, the morphology of the breccia cones is similar to the “blowout faults” and associated “explosion breccias” documented by Montenat et al. (2007), which are interpreted to have formed by hydrofracturing of an indurated layer underlain by sediment with overpressurized pore fluids. As the upward-directed pore-fluid pressure overcame the confining lithostatic pressure, upward fracture and fluid propagation was facilitated by local pore-fluid stress exceeding the compressive rock strength (e.g., Engelder and Lacazette, 1990). Most fluid flux apparently passed through the massive breccia (mBx = cataclastite), where a combination of C1 dissolution,

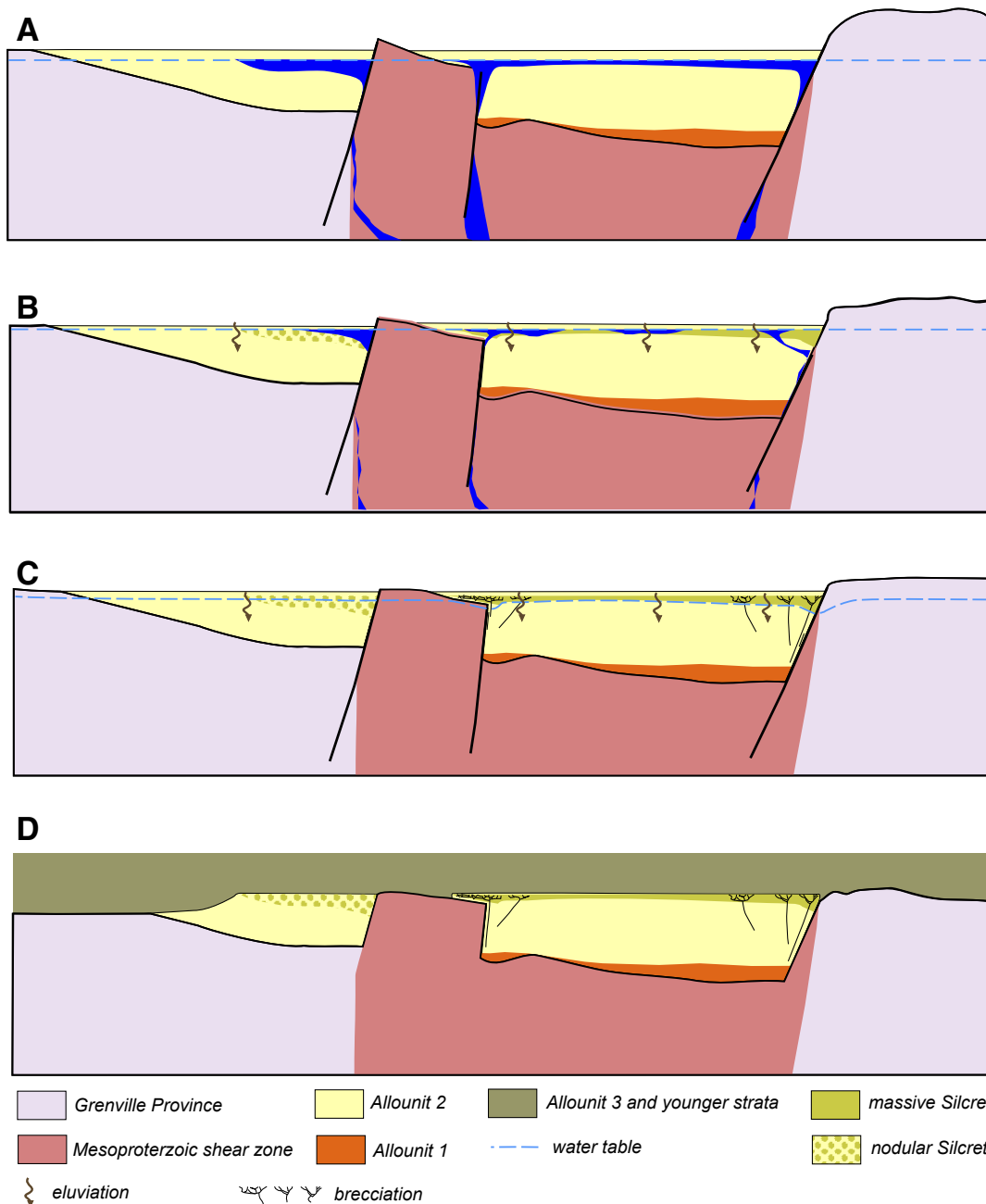


Figure 18. Cross-sectional schematic model outlines the evolution of the silcrete. (A) C1 deposition coincided with the initial upward migration of silica-bearing brines along the Black Lake Shear Zone. The brines entered adjacent Potsdam strata and ponded along the water table, precipitating silcrete. (B) Later C1.5 coincided with a later migration event, coeval with ongoing erosion and eluviation–illuviation. (C) Brecciation coincided with localized escape of pore fluids trapped beneath the relatively impermeable silcrete horizon and possibly with renewed fault motion and brine migration. (D) During the Late Cambrian, the silcrete acted to preserve Allounit 2 strata. Later burial led to pressure solution of quartz in underlying and adjacent Potsdam strata that provided silica for later void-filling C2 overgrowths.

disaggregation, and shear stress from pressurized fluid resulted in nearly complete disaggregation except for remnant disorganized “survivor clasts” that appear to have mostly collapsed into the massive breccia matrix (Fig. 8). The differences noted in overall breccia form from conical to sheet-like were probably controlled by differences in stress regime, with a likely component of horizontal shear in the thinner, sheet-like breccias isolated between the Chippewa Bay and Wellesley Island faults. The dissolution of C1 quartz overgrowths coinciding with fracturing and brecciation suggests that fluids were undersaturated with respect to silica and could have been hot, high pH crustal brines like those associated with C1 and C1.5.

Post-Brecciation: Erosion, Compaction, and Pressure Solution (C2)

Following silcrete formation and brecciation, much of Allounit 2 strata across the Frontenac Arch were eroded during Late Cambrian and earliest Ordovician basin inversion (Lowe et al., 2018; Fig. 18). The silcrete horizon acted as a local well-indurated cap that prevented the erosion of Allounit 2 strata south of the Wellesley Island fault (Figs. 4–5). Succeeding Early Ordovician epeiric seaway transgression over the St. Lawrence Rift system led to clastic and carbonate marine sedimentation that continued until at least the Late Ordovician and buried Potsdam strata to a depth of at least ~1 km (Sanford and Arnott, 2010; Bédard et al., 2018). The pressure solution contacts observed throughout Allounit 2 (Fig. 12B) and at the base of the silcrete nodules (Fig. 10C) most likely occurred during this time. Pressure solution in quartz arenite typically occurs at depths of >2.5 km and temperatures of 90 °C–130 °C; the dependence on temperature can cause pressure solution at shallower depths (Worden and Morad, 2000). Notably, detrital zircon (U-Th)/He thermochronological modeling by Hardie et al. (2017) demonstrates that the Potsdam strata reached temperatures of ~100 °C–130 °C by the Devonian, which suggests either burial depths of >2.5 km or an elevated geothermal gradient that facilitated pressure solution. The latter is more likely given the absence of evidence of post-Ordovician sedimentation in this part of the St. Lawrence Rift system. Dissolved silica from pressure solution of detrital quartz in Allounit 2 strata was then preferentially transported by pore fluids to the relatively porous and uncompactated silcrete horizon, where C2 quartz overgrowths precipitated over earlier C1 ± C1.5 cements and occluded much of the remaining porosity. This proposed transport mechanism is consistent with petrographic and geochemical evidence from numerous similar sedimentary basin burial environments suggesting that silica is commonly transported from one clastic unit to another during burial diagenesis (Houseknecht, 1984; Gluyas and Coleman, 1992; Trewin and Fallick, 2000).

SUMMARY AND CONCLUSIONS

The groundwater silcrete horizon described here locally caps one of three unconformity-bound allounits in Upper Cambrian strata of the Potsdam Group,

along the southernmost exposed extension of the St. Lawrence Rift system exposed along the Frontenac Arch, which lies south of the St. Lawrence River. Here, silcrete texture and thickness strongly support a connection between faulting and silification through the thickening of massive horizons adjacent to Paleozoic faults and underlying Mesoproterozoic shear zones, brecciation near where brittle faults intersect shear zones, and nodules near the margins of shear zones.

Petrography and CL microscopy demonstrate that silcrete consists of three generations of quartz overgrowths. The earliest two, termed C1 and C1.5, are associated with silcrete formation. Fluid inclusion microthermometry from primary fluid inclusion assemblages trapped in C1 overgrowths suggests that silica precipitated from heated saline crustal brines sourced at depth from the Grenville basement, which supports textural and thickness observations from the field suggesting that silicifying fluids migrated along reactivated shear zones. These fluids are envisaged to have then entered the shallow Potsdam aquifer and ascended to the water table, where decreasing temperature and pH promoted quartz precipitation. Differences in silcrete form from nodular to massive reflect differences in brine flux into the Potsdam aquifer, with nodules forming at the edge of the shear zones where flux was lower, and massive horizons forming directly over shear zones where flux was higher. In areas where shallow Paleozoic faults intersect Mesoproterozoic shear zones, silcrete formation was followed by localized fracturing and brecciation caused by the violent upward-migration of overpressurized pore fluids below the impermeable massive silcrete.

This silcrete horizon then acted to resist subsequent Late Cambrian erosion, and also acted to preserve pre-compaction intergranular pore space during Ordovician burial. The latest generation of overgrowth cement, C2, was sourced from silica dissolved by pressure solution of detrital quartz in underlying and adjacent Potsdam strata and precipitated preferentially in the uncompacted and porous silcrete.

This example of groundwater silcrete highlights a unique case example with crustal silica sources and fluid migration along faults. Notably, unlike the research reported here, the documented examples that form the basis of the existing near-surface groundwater silcrete model (e.g., Thiry et al., 1988) have not been tested by detailed CL microscopy or fluid inclusion thermometry to constrain silcrete paragenesis or fluid sources. The possibility that many such groundwater silcretes precipitated from crustal brines thus expands the model of groundwater silcrete to include a new type—here termed brine silcrete—that could provide a basis for identifying evidence of syn-sedimentary deformation in similar tectonically active basins.

APPENDIX: TABLES

Provided here are data tables including locations of sections and fluid inclusion microthermometry data. Table A1 provides location data, silcrete thickness, texture, and corresponding samples. Table A2 is the raw fluid inclusion data, including thermometry data, calculated salinities, and fluid inclusion assemblages.

TABLE A1. OUTCROP AND SAMPLE LOCATIONS

Station	X*	Y*	Thickness (cm)	Type/textures	Representative samples
52	404090E	4934500N	48	massive	
78	445882E	4922357N	142	massive+brecciated	
79	446373E	4922953N	117	massive+brecciated	
81	443393E	4918878N	45	massive	
82	443719E	4919166N	37	massive	
84	442480E	4917865N	15	massive+brecciated	
85	441971E	4916836N	20	massive	
86	437384E	4917814N	75	massive+brecciated	86-D, 86-G
87	439288E	4924031N	15	brecciated	87-A
88	438760E	4925121N	23	brecciated	
95	440606E	4915124N	36	massive	
98	433100E	4906750N	75	massive	
100	432072E	4912176N	66	massive	
102	438315E	4919418N	57	massive	
103	438570E	4919804N	105	massive	
104	440433E	4921840N	50	massive+brecciated	104-A
111	439278E	4919731N	72	massive	
113	428485E	4910354N	87	massive	
117	419813E	4907507N	110	nodular	117-N
118	419304E	4907018N	120	nodular	118-A, 118-B
125	438709E	4902532N	23	massive	
130	434488E	4897850N	45	massive+brecciated	
212	438023E	4895608N	90	massive+brecciated	
213	438224E	4895489N	47	massive	
215	440768E	4905993N	8	massive	

*Coordinates are in NAD83 UTM Zone 18.

TABLE A2. FLUID INCLUSION DATA (continued)

Sample	T _h (°C)	T _e (°C)	T _m ice (°C)	T _{m_{hh}} (°C)	Eq. wt% NaCl*	wt% NaCl†	wt% CaCl ₂ †	Fluid inclusion assemblage (FIA)
118A	125.6	-53.2	-25.3	-39.7	25.76	2.64	20.66	FIA4
118A	122.9		-25.9					FIA4
118A	129							FIA4
118A	120.2							FIA4
118A	124.3							FIA4
118A	140.1	-53	-24	-38.5	24.96	2.86	19.89	FIA5
118A	142.3	-55.7	-30.1					FIA5
118A	138.7		-29					FIA5
118A	142.5							FIA5
118A	151.6							FIA6
118A	139.2	-52.6	-26.3	-36.8	26.37	3.49	20.36	FIA5
118A	150		-26.9					FIA6
118A	144.1							FIA6
118A	143.7		-26.5					FIA6
118A	147.2							FIA6
118A	145							FIA6
118A	140.3							FIA5
118B	127.5	-52.6	-26.2					FIA7
118B	129.7		-25.8					FIA7
118B	128							FIA7
118B	143.2		-25.2					FIA8
118B	140.6	-53	-23.2					FIA8
118B	144.1		-23.6					FIA10
118B	140							FIA8
118B	141.1	-52.8						FIA8
118B	150.2	-53	-28.1	-38	27.48	3.23	21.37	FIA9
118B	143.9							FIA9
86G	132.9	-54.3	-26.4					FIA11
86G	140.9		-27.3					FIA12
86G	134.2							FIA11
86G	139.3	-55.1	-27.9	-37.1	27.35	3.50	21.05	FIA12
86G	133.1		-28.1					FIA11
86G	136.4							FIA13
86G	132.9	-54.2	-28.2	-37.1	27.54	3.51	21.17	FIA11
86G	139.8	-54.5	-27.5		27.11			FIA12
86G	136.5							FIA13
86G	140.1		-26.6					FIA12
86G	139.6	-53.6	-26.5	-38.1	26.50	3.11	20.78	FIA14
86G	137.2		-26.1					FIA14
86G(dup)	135		-31					FIA15
86G(dup)	139.2	-53.6	-31.2	-40.1	29.43	2.83	22.94	FIA15
86G(dup)	132.6		-30.6		29.04			FIA15
86G(dup)	134							FIA15
86G(dup)	136							FIA15

Note: T_h—homogenization temperature, T_e—eutectic temperature, T_m ice—melting temperature of water ice, T_{m_{hh}}—melting temperature of hyrohalite.

*Calculated using equation of Bodnar (1993).

†Calculated using spreadsheet of Steele-MacInnis et al. (2011) for the H₂O–NaCl–CaCl₂ system.

(continued)

ACKNOWLEDGMENTS

This work was supported by a Natural Sciences and Engineering Research Council of Canada Discovery Grant to R.W.C. Arnott. We acknowledge the memory and pioneering work of Bruce Selleck and Bruce Sanford in this region, without which this work on the Potsdam and St. Lawrence Rift system would not be feasible. Thank you also to the two anonymous reviewers for their constructive comments that ultimately improved the clarity and impact of this manuscript.

REFERENCES CITED

- Allaz, J., Selleck, B., Williams, M.L., and Jercinovic, M.J., 2013, Microprobe analysis and dating of monazite from the Potsdam Formation, New York: A progressive record of chemical reaction and fluid interaction: *American Mineralogist*, v. 98, p. 1106–1119, <https://doi.org/10.2138/am.2013.4304>.
- Allen, J.S., Thomas, W.A., and Lavoie, D., 2010, The Laurentian margin of northeastern North America, in Tollo, R., Bartholelew, M.J., Hibbard, J.P., and Karabinos, P.M., eds., *Rodinia to Pangea: The Lithotectonic Record of the Appalachian Region*: Geological Society of America Memoir 206, p. 71–90, [https://doi.org/10.1130/2010.206\(04\)](https://doi.org/10.1130/2010.206(04)).
- Bédard, K., Comeau, F.A., Raymond, J., Malo, M., and Nasr, M., 2018, Geothermal characterization of the St. Lawrence Lowlands sedimentary basin, Québec, Canada: *Natural Resources Research*, v. 27, p. 479–502, <https://doi.org/10.1007/s11053-017-9363-2>.
- Bertotti, G., Seward, D., Wijbrans, J., ter Voorde, M., and Hurford, A.J., 1999, Crustal thermal regime prior to, during, and after rifting: A geochronological modeling study of the Mesozoic South Alpine rifted margin: *Tectonics*, v. 18, no. 2, p. 185–200, <https://doi.org/10.1029/1998TC900028>.
- Blum, A.E., and Stillings, L.L., 1995, Feldspar dissolution kinetics, in White, A.F., and Brantley, S.L., eds., *Chemical Weathering Rates of Silicate Minerals: Reviews in Mineralogy*, v. 31, p. 291–352, <https://doi.org/10.1515/9781501509650>.
- Bohdan, R.J., 1993, Revised equation and table for determining the freezing point depression of H₂O-NaCl solutions: *Geochimica et Cosmochimica Acta*, v. 57, no. 3, p. 683–684, [https://doi.org/10.1016/0016-7037\(93\)90378-A](https://doi.org/10.1016/0016-7037(93)90378-A).
- Bohdan, R.J., Lecumberri-Sánchez, P., Moncada, D., and Steele-Maclennan, M., 2014, Fluid inclusions in hydrothermal ore deposits, in Holland, H.D., and Turekian, K.K., eds., *Treatise on Geochemistry* (second edition), v. 13: Oxford, UK, Elsevier, p. 119–142.
- Carpenter, A.B., Trout, M.L., and Pickett, E.E., 1974, Preliminary report on the origin and chemical evolution of lead- and zinc-rich oil field brines in Central Mississippi: *Economic Geology*, v. 69, no. 8, p. 1191–1206, <https://doi.org/10.2113/gsecongeo.69.8.1191>.
- Cawood, P.A., McCausland, P.J.A., and Dunning, G.R., 2001, Opening Iapetus: Constraints from the Laurentian margin in Newfoundland: *Geological Society of America Bulletin*, v. 113, no. 4, p. 443–453, [https://doi.org/10.1130/0016-7606\(2001\)113<0443:OICFTL>2.0.CO;2](https://doi.org/10.1130/0016-7606(2001)113<0443:OICFTL>2.0.CO;2).
- Crough, S.T., 1981, Mesozoic hotspot epeirogeny in eastern North America: *Geology*, v. 9, no. 1, p. 2–6, [https://doi.org/10.1130/0091-7613\(1981\)9<2:MHEIEN>2.0.CO;2](https://doi.org/10.1130/0091-7613(1981)9<2:MHEIEN>2.0.CO;2).
- Dove, P.M., and Elston, S.F., 1992, Dissolution kinetics of quartz in sodium chloride solutions: Analysis of existing data and a rate model for 25°C: *Geochimica et Cosmochimica Acta*, v. 56, no. 12, p. 4147–4156, [https://doi.org/10.1016/0016-7037\(92\)90257-J](https://doi.org/10.1016/0016-7037(92)90257-J).
- Dove, P.M., and Rimstidt, J.D., 1994, Silica-water interactions: *Reviews in Mineralogy*, v. 29, p. 259–308.
- Engelder, T., and Lacazette, A., 1990, Natural hydraulic fracturing, in Barton, N., and Stephansson, O., eds., *Rock Joints*: Rotterdam, The Netherlands, A.A. Balkema, p. 35–43.
- Fall, A., and Bodnar, R.J., 2018, How precisely can the temperature of a fluid event be constrained using fluid inclusions?: *Economic Geology*, v. 113, no. 8, p. 1817–1843, <https://doi.org/10.5382/econgeo.2018.4614>.
- Frelinger, S.N., Ledvina, M.D., Kyle, J.R., and Zhao, D., 2015, Scanning electron microscopy cathodoluminescence of quartz: Principles, techniques and applications in ore geology: *Ore Geology Reviews*, v. 65, p. 840–852.
- Gall, Q., Davis, W.J., Lowe, D.G., and Dabros, Q., 2017, Diagenetic apatite character and in situ ion microprobe U-Pb age, Keeseville Formation, Potsdam Group, New York State: *Canadian Journal of Earth Sciences*, v. 54, no. 7, p. 785–797.
- Gillard, A.J., Hebert, L.I., Javier-Jimenez, D.R., Masi, J.M., Meyler, S.R., Schwartz, S.G., Verhaeg, E.A., Hughes, J.M., Lincoln, E.S., O'Brien, G.P., Powers, S.K., Schireman, R.G., Lupulescu, M.V., and Bailey, D.G., 2021, Chlorine-rich amphiboles from the Grenville-age Hudson Highlands of New York State: *The Canadian Mineralogist*, v. 59, p. 139–148, <https://doi.org/10.3749/canmin.2000052>.
- Gluyas, J., and Coleman, M.L., 1992, Material flux and porosity changes during sediment diagenesis: *Nature*, v. 356, p. 52–54, <https://doi.org/10.1038/356052a0>.
- Goldstein, R.H., 2003, Fluid inclusions, in Middleton, G.V., Church, M.J., Coniglio, M., Hardie, L.A., and Longstaffe, F.J., eds., *Encyclopedia of Sediments and Sedimentary Rocks: Encyclopedia of Earth Sciences Series*: Dordrecht, The Netherlands, Springer, p. 297–300, https://doi.org/10.1007/978-1-4020-3609-5_92.
- Goldstein, R.H., and Reynolds, J.T., 1994, Systematics of Fluid Inclusions in Diagenetic Minerals: SEPM Short Course Notes, v. 31, 199 p., <https://doi.org/10.2110/scn.94.31>.
- Haines, S., Lynch, E., Mulch, A., Valley, J. W., and van der Pluijm, B., 2016, Meteoric fluid infiltration in crustal-scale normal fault systems as indicated by δ¹⁸O and δ^{2H} geochemistry and ⁴⁰Ar/³⁹Ar dating of neofomed clays in brittle fault rocks: *Lithosphere*, v. 8, no. 6, p. 587–600, <https://doi.org/10.1130/L483.1>.
- Hardie, R.A., Schneider, D.A., and Garver, J.I., 2017, (U-Th)/He thermochronology of the Ottawa Embayment, Eastern Canada: The temperature-time history of an ancient, intracratonic rift basin: *The Journal of Geology*, v. 125, no. 6, p. 659–680, <https://doi.org/10.1086/693859>.
- Hogarth, D.D., Rushforth, P., and McCormick, R.H., 1988, The Blackburn carbonatites, near Ottawa, Ontario: Dikes with fluidized emplacement: *Canadian Mineralogist*, v. 26, p. 377–390.
- Hollingsworth, A.D., Koehn, D., Dempster, T.J., and Aanyu, K., 2019, Structural controls on the interaction between basin fluids and a rift flank fault: Constraints from the Bwamba Fault, East African Rift: *Journal of Structural Geology*, v. 118, p. 236–249, <https://doi.org/10.1016/j.jsg.2018.10.012>.
- Hollis, C., Bastesen, E., Boyce, A., Corlett, H., Gauthier, R., Hirani, J., Rottevatn, A., and Whitaker, F., 2017, Fault-controlled dolomitization in a rift basin: *Geology*, v. 45, p. 219–222, <https://doi.org/10.1130/G38s394.1>.
- Houseknecht, D.W., 1984, Influence of grain size and temperature on intergranular pressure solution, quartz cementation, and porosity in a quartzose sandstone: *Journal of Sedimentary Petrology*, v. 54, no. 2, p. 348–361, <https://doi.org/10.1306/212F8418-2B24-11D7-8648000102C1865D>.
- Kamo, S.L., Krogh, T.E., and Kumarapeli, P.S., 1995, Age of the Grenville dyke swarm, Ontario-Quebec: Implications for the timing of Iapetan rifting: *Canadian Journal of Earth Sciences*, v. 32, no. 3, p. 273–280.
- Kendrick, K.J., and Graham, R.C., 2004, Pedogenic silica accumulation in chronosequence soils: Southern California: *Soil Science Society of America Journal*, v. 68, no. 4, p. 1295–1303.
- Khalaf, F.I., 1988, Petrography and diagenesis of silcrete from Kuwait, Arabian Gulf: *Journal of Sedimentary Petrology*, v. 58, no. 6, p. 1014–1022.
- Kumarapeli, P.S., and Saul, V.A., 1966, The Saint Lawrence valley system: A North American equivalent of the East African Rift valley system: *Canadian Journal of Earth Sciences*, v. 3, no. 5, p. 639–658.
- Kumarapeli, S., Pintson, H., and Dunning, G.R., 1989, Age of the Tibbit Hill Formation and its implications on the timing of Iapetan rifting: *Geological Association of Canada—Mineralogical Association of Canada Joint Annual Meeting Program with Abstracts*, v. 14, p. 125.
- Lampe, C., Person, M., Noeth, S., and Ricken, W., 2002, Episodic fluid flow within continental rift basins: Some insights from field data and mathematical models of the Rhinegraben: *Geofluids*, v. 1, no. 1, p. 42–52, <https://doi.org/10.1046/j.1468-8123.2001.11005.x>.
- Lewis, T.L., 1963, A paleocurrent study of the Potsdam Sandstone of New York, Quebec, and Ontario [Ph.D. thesis]: Ohio State University, 174 p.
- Lowe, D.G., and Arnott, R.W.C., 2016, Composition and architecture of braided and sheetflood-dominated ephemeral fluvial strata in the Cambrian–Ordovician Potsdam Group: A case example of the morphodynamics of early Phanerozoic fluvial systems and climate change: *Journal of Sedimentary Research*, v. 86, no. 6, p. 587–612, <https://doi.org/10.2110/jsr.2016.39>.
- Lowe, D.G., Arnott, R.W.C., Nowlan, G.S., and McCracken, A.D., 2017, Lithostratigraphic and allostratigraphic framework of the Cambrian–Ordovician Potsdam Group and correlations across Early Paleozoic southern Laurentia: *Canadian Journal of Earth Sciences*, v. 54, p. 550–585, <https://doi.org/10.1139/cjes-2016-0151>.
- Lowe, D.G., Arnott, R.W.C., Chiarenzelli, J.R., and Rainbird, R.H., 2018, Early Paleozoic rifting and reactivation of a passive-margin rift: Insights from detrital zircon provenance signatures of the Potsdam Group, Ottawa Graben: *Geological Society of America Bulletin*, v. 130, no. 7–8, p. 1377–1396, <https://doi.org/10.1130/B31749.1>.
- McCausland, P.J.A., Hankard, F., Van der Voo, R., and Hall, C.M., 2011, Ediacaran paleogeography of Laurentia: Paleomagnetism and ⁴⁰Ar/³⁹Ar geochronology of the 583 Ma Baie des Moutons syenite, Quebec: *Precambrian Research*, v. 187, p. 58–78.
- McHone, J.G., and Butler, J.R., 1984, Mesozoic igneous provinces of New England and the opening of the North Atlantic Ocean: *Geological Society of America Bulletin*, v. 95, no. 7, p. 757–765, [https://doi.org/10.1130/0016-7606\(1984\)95<757:MIPONE>2.0.CO;2](https://doi.org/10.1130/0016-7606(1984)95<757:MIPONE>2.0.CO;2).

- Miles, A.R., and Thiry, M., 1992, Silcretes, in Martini, I.P., and Chesworth, W., eds., Weathering, Soils and Paleosols: Developments in Earth Surface Processes 2: Amsterdam, Elsevier, p. 349–377.
- Montenat, C., Barrier, P., Ott d'Estevou, P., and Hibsch, C., 2007, Seismites: An attempt at critical analysis and classification: *Sedimentary Geology*, v. 196, no. 1–4, p. 5–30, <https://doi.org/10.1016/j.sedgeo.2006.08.004>.
- Morey, G.W., Fournier, R.O., and Rowe, J.J., 1962, The solubility of quartz in water in the temperature interval from 25° to 300° C: *Geochimica et Cosmochimica Acta*, v. 26, no. 10, p. 1029–1043, [https://doi.org/10.1016/0016-7037\(62\)90027-3](https://doi.org/10.1016/0016-7037(62)90027-3).
- Nash, D.J., and Ullyott, J.S., 2007, Silcrete, in Nash, D.J., and McLaren, S.J., eds., *Geochemical Sediments and Landscapes*: Oxford, UK, Blackwell Publishing, p. 95–148.
- Nash, D.J., McLaren, S.J., and Webb, J.A., 2004, Petrology, geochemistry and environmental significance of silcrete-calcrete intergrade duricrusts at Kang Pan and Tswaane, central Kalahari, Botswana: *Earth Surface Processes and Landforms*, v. 29, no. 12, p. 1559–1586, <https://doi.org/10.1002/esp.1138>.
- Njinju, E.A., Kolawole, F., Atekwana, E.A., Stamps, D.S., Atekwana, E.A., Abdelsalam, M.G., and Mickus, K.L., 2019, Terrestrial heat flow in the Malawi rifted zone, East Africa: Implications for tectono-thermal inheritance in continental rift basins: *Journal of Volcanology and Geothermal Research*, v. 387, <https://doi.org/10.1016/j.jvolgeores.2019.07.023>.
- Otvos, E.G., Jr., 1966, Sedimentary structures and depositional environments, Potsdam Formation, Upper Cambrian: *American Association of Petroleum Geologists Bulletin*, v. 50, no. 1, p. 159–165.
- Pryor, W.A., 1973, Permeability-porosity patterns and variations in some Holocene sand bodies: *American Association of Petroleum Geologists Bulletin*, v. 57, no. 1, p. 162–189.
- Raiswell, R., and Fisher, Q.J., 2000, Mudrock-hosted carbonate concretions: A review of growth mechanisms and their influence on chemical and isotopic composition: *Journal of the Geological Society, London*, v. 157, Part 1, p. 239–251, <https://doi.org/10.1144/jgs.157.1.239>.
- Rimando, R.E., and Benn, K., 2005, Evolution of faulting and paleo-stress field within the Ottawa Graben, Canada: *Journal of Geodynamics*, v. 39, no. 4, p. 337–360, <https://doi.org/10.1016/j.jog.2005.01.003>.
- Salad Hersi, O., and Dix, G.R., 2006, Precambrian fault systems as control on regional differences in relative sea level along the Early Ordovician platform of eastern North America: *Journal of Sedimentary Research*, v. 76, no. 3–4, p. 700–716, <https://doi.org/10.2110/jsr.2006.016>.
- Sanford, B.V., and Arnott, R.W.C., 2010, Stratigraphic and structural framework of the Potsdam Group in eastern Ontario, western Quebec, and northern New York State: *Geological Survey of Canada Bulletin* 597, 83 p.
- Selleck, B., 2005, Trip A-2: Exploring the root zone of an ancient fault-driven hydrothermal system in the Adirondack Lowlands, New York: *New York State Geological Association Meeting Guidebook*, v. 77, p. 11–28.
- Selleck, B.W., 1978, Syndepositional brecciation in the Potsdam Sandstone of northern New York State: *Journal of Sedimentary Petrology*, v. 48, no. 4, p. 1177–1184.
- Selley, R.C., 1978, Porosity gradients in North Sea oil-bearing sandstones: *Journal of the Geological Society*, v. 135, p. 119–132, <https://doi.org/10.1144/gsjgs.135.1.0119>.
- Shaw, P.A., and Nash, D.J., 1998, Dual mechanisms for the formation of fluvial silcretes in the distal reaches of the Okavango Delta fan, Botswana: *Earth Surface Processes and Landforms*, v. 23, no. 8, p. 705–714, [https://doi.org/10.1002/\(SICI\)1096-9837\(199808\)23:8<705::AID-ESP875>3.0.CO;2-7](https://doi.org/10.1002/(SICI)1096-9837(199808)23:8<705::AID-ESP875>3.0.CO;2-7).
- Shepherd, T.J., Rankin, A.H., and Alderton, D.H.M., 1985, *A Practical Guide to Fluid Inclusion Studies*: Glasgow and London, Blackie and Son Ltd., 237 p.
- Steele-MacInnis, M.J., Bodnar, R.J., and Naden, J., 2011, Numerical model to determine the composition of H_2O -NaCl-CaCl₂ fluid inclusions based on microthermometric and micro-analytical data: *Geochimica et Cosmochimica Acta*, v. 75, no. 1, p. 21–40, <https://doi.org/10.1016/j.gca.2010.10.002>.
- Summerfield, M.A., 1983, Petrography and diagenesis of silcrete from the Kalahari Basin and Cape coastal zone, Southern Africa: *Journal of Sedimentary Petrology*, v. 53, no. 3, p. 895–909, <https://doi.org/10.1306/212F82E2-2B24-11D7-8648000102C1865D>.
- Thiry, M., 1999, Diversity of continental silification features: Examples from the Cenozoic deposits in the Paris Basin and neighbouring basement, in Thiry, M., and Simon-Colcon, R., eds., *Paleoweathering, Paleosurfaces, and Related Continental Deposits: Special Publication of the International Association of Sedimentologists* 27: Hoboken, New Jersey, Wiley-Blackwell, p. 87–127.
- Thiry, M., and Milnes, A.R., 1991, Pedogenic and groundwater silcretes at Stuart Creek opal field, South Australia: *Journal of Sedimentary Petrology*, v. 61, no. 1, p. 111–127.
- Thiry, M., Ayrault, M.B., and Grisoni, J.-C., 1988, Ground-water silification and leaching in sands: Example of the Fontainebleau Sand (Oligocene) in the Paris Basin: *Geological Society of America Bulletin*, v. 100, no. 8, p. 1283–1290, [https://doi.org/10.1130/0016-7606\(1988\)100<1283:GWSALI>2.3.CO;2](https://doi.org/10.1130/0016-7606(1988)100<1283:GWSALI>2.3.CO;2).
- Trewin, N.H., and Fallick, A.E., 2000, Quartz cement origins and budget in the Tumblagooda Sandstone, Western Australia, in Worden, R.H., and Morad, S., *Quartz Cementation in Sandstones: Special Publication of the International Association of Sedimentologists* 29: Hoboken, New Jersey, Wiley-Blackwell, p. 219–229, <https://doi.org/10.1002/9781444304237.ch15>.
- Warner, N.R., Jackson, R.B., Darragh, T.H., Osborn, S.G., Down, A., Zhao, K., White, A., and Vengosh, A., 2012, Geochemical evidence for possible natural migration of Marcellus Formation brine to shallow aquifers in Pennsylvania: *Proceedings of the National Academy of Sciences of the United States of America*, v. 109, no. 30, p. 11961–11966, <https://doi.org/10.1073/pnas.1121181109>.
- Webb, J.A., and Golding, S.D., 1998, Geochemical mass-balance and oxygen-isotope constraints on silcrete formation and its paleoclimatic implications in southern Australia: *Journal of Sedimentary Research*, v. 68, no. 5, p. 981–993, <https://doi.org/10.2110/jsr.68.981>.
- Whelan, J.F., Rye, R.O., De Lorraine, W., and Ohmoto, H., 1990, Isotopic geochemistry of a mid-Proterozoic evaporite basin: *American Journal of Science*, v. 290, p. 396–424, <https://doi.org/10.2475/ajs.290.4.396>.
- Wilkinson, J.J., 2017, Metastable freezing: A new method for the estimation of salinity in aqueous fluid inclusions: *Economic Geology*, v. 112, no. 1, p. 185–193, <https://doi.org/10.2113/econgeo.112.1.185>.
- Wolf, R.R., and Dalrymple, R.W., 1984, Sedimentology of the Cambro-Ordovician sandstones of eastern Ontario, in *Geoscience Research Grant Program, Summary of Research, 1984–1985: Ontario Geological Survey Miscellaneous Paper* 121, p. 240–252.
- Wong, M.S., Peck, W.H., Selleck, B.W., Catalano, J.P., Hochman, S.D., and Maurer, J.T., 2011, The Black Lake Shear Zone: A boundary between terranes in the Adirondack Lowlands, Grenville Province: *Precambrian Research*, v. 188, no. 1–4, p. 57–72, <https://doi.org/10.1016/j.precamres.2011.04.001>.
- Worden, R.H., and Morad, S., 2000, Quartz cementation in oil field sandstones: A review of the key controversies, in Worden, R.H., and Morad, S., eds., *Quartz Cementation in Sandstones: Special Publication of the International Association of Sedimentologists* 29: Hoboken, New Jersey, Wiley-Blackwell, p. 1–20, <https://doi.org/10.1002/9781444304237.ch1>.
- Yardley, B.W.D., and Bodnar, R.J., 2014, Fluids in the continental crust: *Geochemical Perspectives*, v. 3, p. 1–127, <https://doi.org/10.7185/geochempersp.3.1>.